ELSEVIER

Contents lists available at ScienceDirect

Biomedical Signal Processing and Control

journal homepage: www.elsevier.com/locate/bspc





MitoSkel: AI tool for semantic segmentation and quantification of mitochondria from light microscopy images

Soumaya Zaghbani a,b,* Rubaiya Kabir Pranti a, Lukas Faber a, Ana J. Garcia-Saez a,b

- a Institute of Genetics, CECAD, University of Cologne, Cologne, Germany
- ^b Max Planck Institute of Biophysics, Frankfurt am Main, Germany

ABSTRACT

Mitochondria are cellular organelles regulating key processes, including metabolism, calcium signaling and cell death. They form an intricate tubular network in cells whose shape is tightly associated with function and that can be readily visualized with fluorescence microscopy. However, accurately quantifying mitochondrial morphology from light microscopy images remains a complex task, which underscores the need for an efficient and user-friendly tool for automatically detecting and analyzing the organelles morphology. Here, we introduce a novel artificial intelligence-based system for automatic mitochondria segmentation and quantification called MitoSkel utilizes a new architecture of U-Net that we call GAU-Net, which integrates a trainable Gabor filter layer and a Thresholding Attention Mechanism (TAM). We trained GAU-Net on a comprehensive dataset of fluorescence microscopy images to perform pixel-level segmentation of mitochondria under various conditions. Following segmentation, MitoSkel applies skeletonization to extract the morphological features of individual mitochondria, facilitating the quantification of parameters such as length, branching points, and connectivity. Thorough evaluation across diverse cell lines imaged using different microscopy methods demonstrates the proficiency of MitoSkel in handling varying mitochondrial shapes, sizes, and densities. Compared to existing methods, our approach achieved improved segmentation accuracy and efficiency. MitoSkel promises to be a valuable tool for the study of mitochondrial shape and its connection with organelle dynamics, function and related diseases.

1. Introduction

Mitochondria are organelles in eukaryotic cells that play a central role not only in energy production, but also in cellular metabolism, calcium signaling, cell death regulation and immunity [1]. They form a tubular network in the cell, whose shape responds to mitochondrial function and fitness through still poorly understood mechanisms. Furthermore, alterations in mitochondrial shape have been associated with diseases [1,2]. For these reasons, mitochondrial research often requires analysis of the network morphology [3]. This is routinely done with fluorescence microscopy, which offers real-time imaging capabilities, ease of use, versatility, and suitability for live-cell studies [4]. Analysis of mitochondria using accurate segmentation of the images is of interest for the research community because it can provide essential insights into cellular functions and contribute significantly to our understanding of diseases related to mitochondria and potential therapeutic intervention [5,6]. However, an accurate quantitative analysis of mitochondrial shape remains a time-consuming and often biased process due to the lack of user-friendly tools for efficient and automatic detection of the organelles from microscopy images. The primary difficulty lies in the highly variable shapes and sizes of mitochondria, which range from elongated tubules to fragmented structures [7]. This variability complicates the development of a standardized segmentation approach. Adding to the complexity, issues like noise, variable illumination, and image artifacts can interfere with accurate segmentation. Batch effects are also issuing in microscopy data, due to systematic variations resulting from factors like temperature fluctuations or differences in microscopy lighting conditions during an experiment. These variations lead to alterations in image intensities and features across different batches [8]. Another challenge is the dense packing of mitochondria within cells, often resulting in overlapping structures that make it hard to distinguish individual mitochondria.

In response to these challenges, researchers in the field of bioimage analysis have developed a range of computational approaches. These methods typically involve a combination of edge detection, region-based algorithms, and machine learning models to segment mitochondria accurately [6,9]. Advanced image pre-processing techniques and 3D imaging also play a crucial role in enhancing segmentation performance [7,10]. Early investigations into mitochondria segmentation and quantification relied on traditional image processing [11–13], limited by noise, the requirement of manual threshold selection and varying image conditions, which resulted in unsatisfactory results [14]. The

E-mail address: szaghban@uni-koeln.de (S. Zaghbani).

^{*} Corresponding authors.

introduction of convolutional neural networks (CNNs), characterized by their unique architecture capable of automatically and adaptively learning spatial hierarchies of features, has revolutionized image recognition and analysis tasks [15]. The U-Net architecture, introduced by Ronneberger et al [16,37], specifically for biomedical image segmentation, features a symmetric expanding path that enabled precise localization, providing enhanced capabilities in capturing the intricate details and variabilities in biological images. U-Net was used in Mito-SegNet to accurately capture the intricate features of mitochondrial shape with a pretrained deep learning (DL) segmentation model [17]. More recently, Ilastik workflows, a collection of machine-learning-based image processing tasks, facilitated semantic segmentation of images with user-defined class labels and improved the separation of foreground from background, allowing further object-level analysis [18].

Here, we leveraged DL, particularly the U-Net architecture [36], to address these challenges and improve automatic mitochondria segmentation from light microscopy images. To enhance the U-net model's ability to capture intricate details, we integrated a trainable Gabor Layer into the base architecture, which allowed the model to detect nuanced patterns and features within the input data. Additionally, we used a Thresholding Attention Mechanism (TAM) to guide the system in prioritizing specific regions of interest within the images. This streamlined the segmentation process and improved the quality of the results by emphasizing relevant areas, thereby significantly enhancing the model's performance. We tested our model on a comprehensive dataset comprising images from four different cell lines acquired through various microscopy techniques and compared it with MitoSegNet and Ilastik. The resulting tool, MitoSkel offers improved performance and can effectively adapt to different cell lines and microscope setups, including both low-resolution and high-resolution configurations, while accommodating diverse experimental conditions.

2. Proposed model

Considering the key role of high-quality datasets in the learning process, we decided to first create a robust and comprehensive dataset aimed at enhancing the generalizability of our system for mitochondria segmentation across a spectrum of diverse shapes and resolutions. To achieve this, we acquired images of cultured U2OS and HeLa cells using confocal, Airy-scan and structured illumination microscopies, each providing images rich in mitochondrial structure and morphology details (see Materials and Methods section). We standardized the sizes of all images to guarantee uniformity and consistency across the dataset Fig. 1A.

We then used these data to train a DL model based on the U-Net architecture. To enhance the accuracy, robustness, and adaptability of the segmentation process, we modified the U-Net model by introducing novel components into the basic architecture. This resulted in a new framework that we called "GAU-Net", which adds two key elements to the basic architecture: Gabor filters [19,20] and a Thresholding Attention Mechanism (TAM). These enhancements tackle the complexities of mitochondria images, where textures, fine details, and the inherent imbalance in information distribution challenge conventional segmentation methods. In the proposed architecture, the Gabor layer is integrated into the network as part of the convolutional blocks, allowing it to learn filter parameters during training. Additionally, a TAM is applied to the output of each convolutional block, enhancing the model's ability to focus on relevant image regions. The encoder part of the GAU-Net architecture comprises four sequential convolutional blocks. Each block consists of a Gabor layer and two convolutional layers, with a ReLu activation function in between, followed by the attention mechanism. This design allows the network to progressively extract hierarchical features from the input data while incorporating Gabor-based feature extraction and attention mechanisms to enhance the model's ability to capture complex patterns and structures in the input images. The decoder portion mirrors this structure, with four corresponding upsampling blocks that progressively increase the spatial dimensions of the feature maps. Skip connections are established between corresponding encoder and decoder blocks to facilitate the flow of high-resolution features during up-sampling. However, unlike the encoder, which includes the Gabor layer, the decoder focuses on reconstructing the original input from the encoded features with deconvolution. The model is described in Fig. 1B.

The Gabor filters, known for their efficacy in capturing spatial frequencies and orientations and their ability to capture texture and fine details in images [21,22], were carefully parameterized to optimize texture and edge detection across various scales and directions. The mathematical formulation of a Gabor filter can be expressed as:

$$Gabor(\lambda, \theta, \phi, \sigma, \gamma) (x_0, y_0) = exp\left(-\frac{{x_0}^2 + \gamma^2 {y_0}^2}{2\sigma^2}\right) \cdot exp\left(i\left(\frac{2\pi x_0}{\lambda} + \phi\right)\right) \tag{1}$$

Where x_0 and y_0 are defined as $x_0 = x\cos\theta + y\sin\theta$ and $y_0 = -x\sin\theta + y\cos\theta$, in which θ defines the orientation of the filter, σ controls the filter's size, λ specifies the wavelength of the sinusoidal component, γ adjusts the spatial aspect ratio and ϕ is phase offset [20-22]. Incorporating Gabor filters into our neural network architecture via an extra trainable layer introduced a mechanism for enriching feature representations. After several tests and iterations, we identified an ideal set of parameters: a sigma (σ) of 2.0 to balance feature breadth and detail, theta (θ) values spaced evenly from 0 to π to ensure comprehensive orientation coverage, a lambda (λ) of 5.0 for effective medium-to-high frequency pattern extraction, a gamma (γ) of 0.2 to highlight elongated structures, and a phase offset (ϕ) of 0, enhancing edge detection. This configuration allowed the model to extract textural and structural information, facilitating precise segmentation. The proposed trainable Gabor layer was used to extract multi-orientation and multi-scale features Fig. 1B. By integrating a trainable Gabor layer into the UNet architecture, our proposed GAU-Net model exhibits improved segmentation performance.

Unlike previous studies [22–24], in which Gabor filters were used primarily for feature extraction, our model integrates Gabor as trainable layer within the architecture. This allows for end-to-end training and adaptive feature learning, enhancing texture feature extraction and segmentation accuracy.

The Gabor filter parameters were initially chosen based on theoretical insights into their roles in capturing image textures and orientations. However, during the training process, these parameters were fine-tuned through a gradient-based optimization process. Specifically, the parameters were set as trainable within the model. This allowed the GAU-Net architecture to adapt these parameters dynamically to best fit the features of the input data, thereby optimizing the segmentation task. The optimization process was guided by the network's loss function, which adjusted the Gabor filter parameters in each training iteration to improve feature extraction capabilities.

The Gabor layer enhances feature extraction by adaptively learning texture and edge features, performs multi-scale analysis for accurate mitochondria delineation, and demonstrates robustness to noise and variations in illumination. Its adaptability allows for fine-tuning filter parameters during training, optimizing responses for the segmentation task at hand. Furthermore, the complementary nature of Gabor features with convolutional features enriches the model's representation of the input data, resulting in more effective segmentation outcomes. In DL, attention mechanisms enable models to focus on specific parts of the input data that are deemed most relevant. These mechanisms dynamically weight the importance of different input features, allowing the model to selectively pay attention to salient information while ignoring irrelevant or noisy inputs[25–27]. The incorporation of attention mechanisms has led to significant improvements in tasks such as natural language processing and image recognition [28,29].

To mitigate the challenges due to noise during the acquisition of

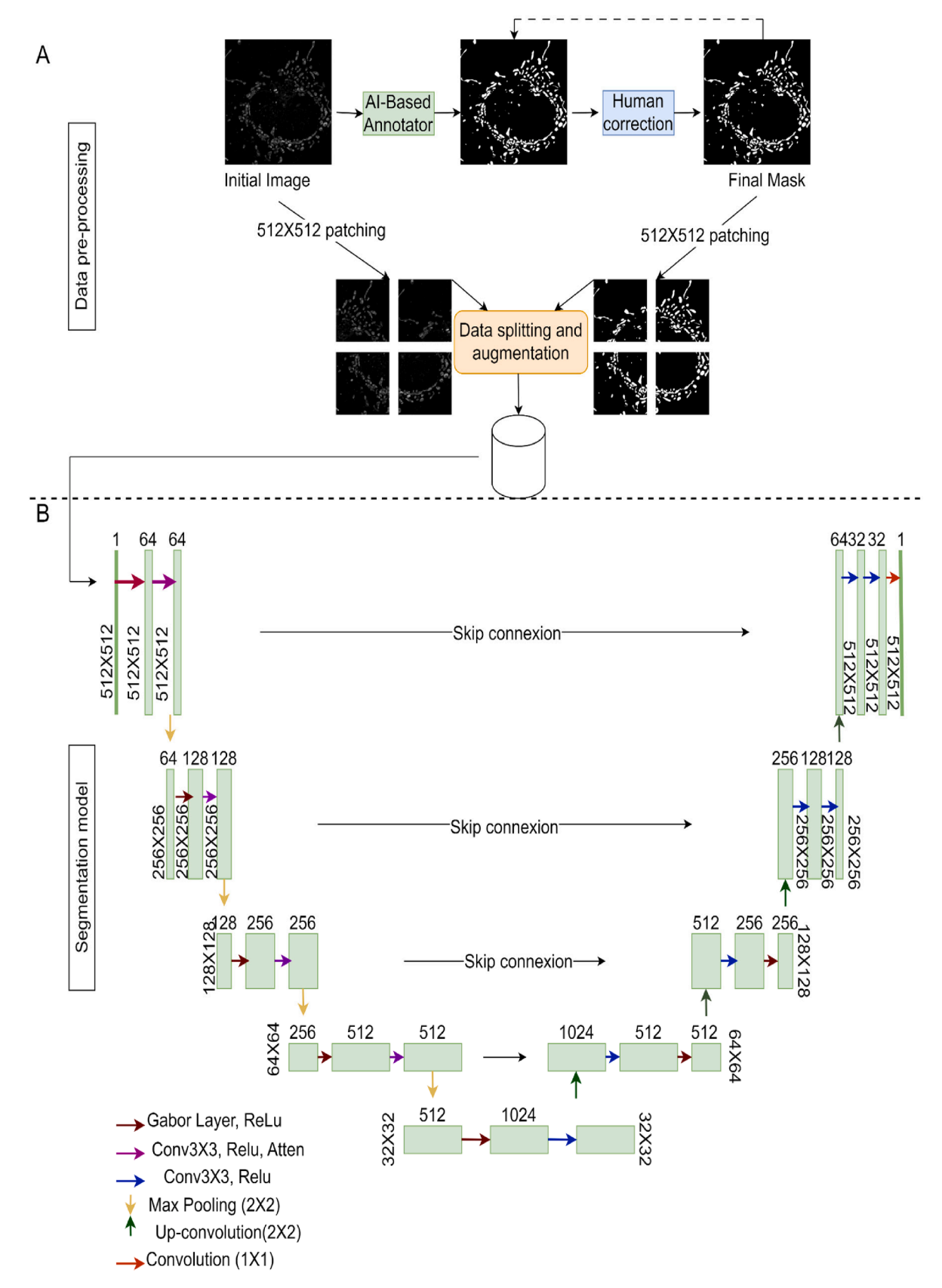


Fig. 1. Pipeline of the proposed model MitoSkel. A. Data Preparation: Ground truths were generated using LabelKit, an AI tool. Subsequently, the images were cropped into 512x512 patches, and the data was split into 70% for training, 10% for validation, and 20% for testing. B. Architecture of GAU-Net: The first block consists of a trainable Gabor layer followed by a ReLU function. The second block comprises a convolutional layer, followed by ReLU and a TAM.

microscopy images, we used a TAM. This mechanism enhances the quality of the acquired images and minimizes noise interference, resulting in cleaner and more accurate data for subsequent analysis and segmentation tasks Fig. 2. The TAM consists of two main components:

Sigmoid Activation: After convolutional processing, the output is passed through a sigmoid activation function to produce an attention map. While sigmoid activation is common, its role in our TAM is to generate a continuous attention map reflecting the relevance of different regions in the image. The input tensor x undergoes convolutional processing represented as:

$$conv(x) = W^*x + b \tag{2}$$

where W is the convolutional weight, x denotes the input tensor, and b represents the bias. Subsequently, the output of this convolution is passed through the sigmoid activation function:

$$attention_{map} = \sigma(conv(x)) = \frac{1}{1 + e^{-conv(x)}}$$
 (3)

The sigmoid activation maps the output to values in the range of 0 to 1, producing an attention map that reflects the network's internal perception of image relevance.

Thresholding Operation: A predefined threshold is applied to this attention map to create a binary mask. This mask highlights the regions with attention values above the threshold, effectively filtering out less relevant parts of the image. This step allows the model to focus on informative areas while suppressing irrelevant or noisy regions.

The binary attention mask is generated by applying a defined threshold to the attention map:

$$\mathit{mask}(i,j) = \left\{ \begin{array}{l} 1, \mathit{ifattention}_{\mathit{map}}(i,j) > \mathit{threshold} \\ 0, \mathit{otherwise} \end{array} \right. \tag{4}$$

The TAM helps to alleviate noise by reducing the influence of nonrelevant areas in the image. By focusing on regions with higher attention values, the TAM ensures that noise or irrelevant details are less likely to interfere with the segmentation process. This selective focus improves the model's ability to segment mitochondria accurately, even in challenging imaging conditions. Once we achieve clear and accurate segmentation of mitochondria, our system can then delineate a contour line around each detected mitochondrion. This sets the basis for accurate quantification of the mitochondrial network. By generating these contours, the system provides insights into various parameters such as area, perimeter, circularity, and thickness, offering a comprehensive and quantitative description of mitochondrial morphology. Furthermore, the system incorporates a skeletonization feature that is applied to the detected mitochondria. This skeletonization process provides additional information about the mitochondrial network, including mitochondrial length, branch connectivity, types of branches, and distances between branches. This dual approach of contouring and skeletonization gives rise to a robust tool for a thorough analysis of mitochondrial structures, facilitating the study of mitochondrial dynamics and their implications in cellular functions.

3. Results

3.1. Segmentation performance

To validate the effectiveness of our approach, we compared our segmentation model, GAU-Net, with other state-of-the-art algorithms U-Net++[30], FCNN[31], SegNet[32], and U-Net[33] and evaluated its performance using a variety of segmentation metrics. These metrics range from 0 to 1, with 1 indicating optimal performance (see Methods and Materials). The benchmarking results highlight the superior performance of GAU-Net relative to other methods across multiple datasets, as shown in Tables 1, 2, and 3. On our custom dataset Table 1, GAU-Net achieved the highest F1 score (0.9689), accuracy (0.9946), IoU (0.9397), precision (0.9796), and specificity (0.9965), outperforming U-Net++, FCNN, SegNet, and U-Net. These results demonstrate GAU-Net's capability to perform domain-specific segmentation tasks with remarkable precision. On the ISIC2018 dataset (Table 2), GAU-Net achieved the highest F1 score (0.8809) and IoU (0.8057), showing improvements over other models. These differences, while small, underline GAU-Net's consistent performance across most metrics and its adaptability to diverse medical imaging challenges. On the Kvasir-SEG dataset (Table 3), GAU-Net achieved F1 score (0.7453) and IoU (0.6040), showcasing its ability to capture fine-grained details. While SegNet (specificity 0.9773) and U-Net (specificity 0.9837) achieved higher specificity, GAU-Net led in F1 score and IoU, metrics critical for overall segmentation performance. These results highlight GAU-Net's ability to outperform existing methods on our custom dataset, where intricate mitochondrial patterns demand advanced edge detection and spatial feature extraction. However, its performance on the ISIC2018 and Kvasir-SEG datasets shows slight variations in certain metrics. This difference can be attributed to the distinct characteristics of the datasets. GAU-Net was primarily designed to focus on patterns with complex and overlapping shapes, where edge and border details are critical for accurate segmentation. This is particularly true for our custom dataset, where mitochondrial structures are intricate, densely packed, and often exhibit significant overlap. The Gabor Layer and TAM in GAU-Net are specifically tailored to enhance segmentation in such challenging scenarios. In contrast, the ISIC2018 and Kvasir-SEG datasets do not share these characteristics. The patterns in these datasets are generally less complex, with clearer boundaries and minimal overlap between structures. Additionally, these datasets feature high-resolution images with

Table 1
Benchmarking GAU-Net: Quantitative Comparison with State-of-the-Art Segmentation Methods on Our Dataset.

Model	F1Score	Accuracy	IoU	Precision	Specificity
UNet++	0.8311	0.9718	0.7110	0.8199	0.9834
FCNN	0.8008	0.9321	0.7056	0.8100	0.9822
SegNet	0.9187	0.9820	0.8616	0.9331	0.9910
U-Net	0.8571	0.9729	0.8603	0.8729	0.9832
GAU-Net	0.9689	0.9946	0,9397	0.9796	0.9965

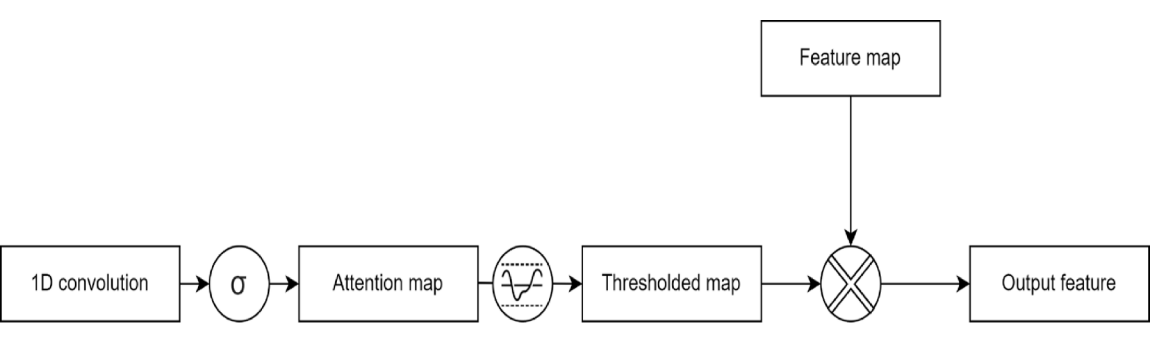


Fig. 2. Diagram of the proposed Thresholding Attention Mechanism (TAM).

Table 2Benchmarking GAU-Net: Quantitative Comparison with State-of-the-Art Segmentation Methods on (ISIC2018 dataset).

Model	F1Score	Accuracy	IoU	Precision	Specificity
Unet++	0.8796	0.9149	0.7843	0.8747	0.9534
FCNN	0.7801	0.8837	0.6509	0.7413	0.8920
SegNet	0.8681	0.9141	0.7332	0.8801	0.9509
U-net	0.8339	0.9101	0.8000	0.8177	0.9458
GAU-Net	0.8809	0.9091	0.8057	0.8848	0.9383

Table 3Benchmarking GAU-Net: Quantitative Comparison with State-of-the-Art Segmentation Methods on Kvasir-SEG dataset.

Model	F1Score	Accuracy	IoU	Precision	Specificity
Unet++	0.7377	0.9201	0.5934	0.7754	0.9214
FCNN	0.5352	0.7959	0.3654	0.4218	0.8080
SegNet	0.7280	0.8782	0.5703	0.6921	0.9773
U-net	0.7395	0.8819	0.5867	0.8819	0.9837
GAU-Net	0.7453	0.9225	0.6040	0.7888	0.9638

minimal acquisition noise, which naturally reduces the need for advanced edge detection or attention mechanisms.

The results in Tables 4, 5, and 6 highlight the impact of incorporating the Gabor Layer and (TAM) on segmentation performance across three datasets: our custom dataset, ISIC2018, and Kvasir-SEG. On our custom dataset (Table 4), the model without the Gabor Layer and TAM (-Gabor/-TAM) achieved an F1 score of (0.9527), accuracy of (0.9927), and IoU of (0.9189). Adding the Gabor Layer (+Gabor/-TAN) resulted in improvements across all metrics, with an F1 score of (0.9615), IoU of (0.9260), and precision of (0.9756). Incorporating TAM without the Gabor Layer (-Gabor/+TAM) achieved slightly better results, with an F1 score of 0(.9626) and IoU of (0.9280). However, the combination of both the Gabor Layer and TAM (+Gabor/+TAN) demonstrated the best performance, with an F1 score of (0.9689), accuracy of (0.9946), IoU of (0.9397), and precision of (0.9796). On the ISIC2018 dataset (Table 5), the baseline model (-Gabor/-TAM) achieved an F1 score of (0.8618), accuracy of (0.9007), and IoU of (0.7728). Adding the Gabor Layer (+Gabor/-TAM) provided improvements, with an F1 score of (0.8757), IoU of (0.7862), and precision of (0.8692). Incorporating TAM without the Gabor Layer (-Gabor/+TAM) resulted in slightly lower IoU (0.7750) and F1 score (0.8626) but improved precision to (0.8800). The full model (+Gabor/+TAN) achieved the best performance, with an F1 score of (0.8809), accuracy of (0.9091), IoU of (0.8057), and precision of (0.8848). On the Kvasir-SEG dataset (Table 6), the baseline model (-Gabor/-TAN) achieved an F1 score of (0.7426), accuracy of (0.9189), and IoU of (0.5905). Adding the Gabor Layer (+Gabor/-TAM) improved segmentation performance, achieving an F1 score of (0.7513), IoU of (0.6017), and precision of (0.7545). Using TAM alone (-Gabor/+TAM)resulted in similar metrics to the baseline, with an F1 score of (0.7432) and IoU of (0.5865). The combination of both the Gabor Layer and TAM (+Gabor/+TAM) achieved the best performance, with an F1 score of (0.7453), accuracy of (0.9925), IoU of (0.6040), and the highest precision of (0.7888). Overall, these results demonstrate that both the Gabor Layer and TAM contribute to improved segmentation performance. While each component individually enhances certain metrics, the

Table 4Comparison of Segmentation results with and without Gabor Layer and Thresholding Attention Mechanism (TAM) (our dataset).

Model	F1Score	Accuracy	IoU	Precision	Specificity
-Gabor/-TAM	0.9527	0.9927	0.9189	0.9713	0.9973
+Gabor/-TAM	0.9615	0.9934	0.9260	0.9756	0.9977
-Gabor/+TAM	0.9626	0.9935	0.9280	0.9729	0.9974
+Gabor/+TAM	0.9689	0.9946	0.9397	0.9796	0.9965

Table 5
Comparison of Segmentation results with and without Gabor Layer and Thresholding Attention Mechanism (TAM) (ISIC2018).

Model	F1Score	Accuracy	IoU	Precision	Specificity
-Gabor/-TAM	0.8618	0.9007	0.7728	0.8660	0.9301
+Gabor/-TAM	0.8757	0.9089	0.7862	0.8692	0.9370
-Gabor/+TAM	0.8626	0.9024	0.7750	0.8800	0.9389
+Gabor/+TAM	0.8809	0.9091	0.8057	0.8848	0.9383

Table 6Comparison of Segmentation results with and without Gabor Layer and Thresholding Attention Mechanism (TAM) (Kvasir-SEG).

Model	F1Score	Accuracy	IoU	Precision	Specificity
-Gabor/-TAM	0.7426	0.9189	0.5905	0.7498	0.9555
+Gabor/-TAM	0.7513	0.9230	0.6017	0.7545	0.9511
-Gabor/+TAM	0.7432	0.9158	0.5865	0.6912	0.9501
+Gabor/+TAM	0.7453	0.9925	0.6040	0.7888	0.9638

combination of both consistently provides the best outcomes across all datasets. The GAU-Net architecture demonstrates its strength in handling segmentation tasks where edge and orientation details are critical, such as in mitochondria segmentation using light microscopy (custom dataset) and gastrointestinal polyp segmentation (Kvasir-SEG dataset). These datasets feature intricate and irregular structures, where the inclusion of the Gabor Layer and TAM enhances the model's ability to capture fine-grained details and spatial features.

The evaluation of the Thresholded Attention Mechanism across different threshold values revealed that a threshold of 0.1 provided the best overall performance. At this threshold, the model achieved the highest F1 score of 0.9615, indicating a superior balance between precision (0.9756) and recall. Additionally, it delivered the highest accuracy of 0.9934, confirming that the model correctly classified the majority of instances. The IoU at this threshold was also the highest (0.9260), reflecting the model's ability to capture significant overlap between predicted and ground truth segmentation (Table 7). Based on these results, the threshold value of 0.1 was consistently applied across all datasets, including our custom dataset, ISIC2018, and Kvasir-SEG, to ensure uniformity in the evaluation and to maximize the model's performance under diverse conditions.

The inclusion of the Gabor Layer and Thresholded Attention Mechanism (TAM) in the GAU-Net architecture enhances segmentation performance with minimal impact on model complexity. The baseline model, without the Gabor Layer and TAM, comprises 12,517,889 parameters, while the combined model (with both components) has 12,647,592 parameters, reflecting a 1.04 % increase in the total parameter count. The Gabor Layer contributes 4 trainable parameters (sigma, theta, lambd, and gamma) and is responsible for edge- and orientation-specific feature extraction, while the TAM adds 129,699 parameters through attention gates, enabling the model to focus on relevant regions and suppress irrelevant features. From a computational efficiency perspective, the combined model increases training and inference time by \sim 6–8 % compared to the baseline. This is due to the additional operations introduced by the Gabor Layer and TAM.

Table 7Segmentation results with different threshold values (our dataset).

Threshold	F1Score	Accuracy	IoU	Precision	Specificity
0.05	0.9518	0.9848	0.9159	0.9677	0.9927
0.15	0.9590	0.9009	0.9223	0.9716	0.9988
0.1	0.9615	0,9934	0,9260	0,9756	0.9977
0.2	0.9413	0.9054	0.9200	0.9423	0.9941

However, this trade-off is justified by the substantial gains in key segmentation metrics, including IoU and F1 score, where the combined model consistently outperforms the baseline across multiple datasets.

3.2. Comparative analysis of mitochondria segmentation systems

Next, we evaluated and compared the performance of our mitochondria segmentation system, MitoSkel, with two other established tools for mitochondria segmentation and analysis: Ilastik and MitoSeg-Net [17,18]. We assessed effectiveness and accuracy in segmenting mitochondria across different cell lines and different microscopes, using a comprehensive range of metrics. Our test dataset included a total of 270 images of the mitochondrial network of individual cells, captured from SIM, Airyscan, and confocal microscopes from different cell lines (see Materials and Methods section). This diverse range of imaging modalities allowed us to assess the robustness and adaptability of the segmentation systems under varying imaging conditions. To achieve this, we refrained from performing any preprocessing on the raw image data. This approach ensured that all systems were evaluated based solely on their intrinsic segmentation capabilities, without any external enhancements or modifications to the original image quality. Furthermore, it is important to note that all images used in our testing were resized to a resolution of 512x512 pixels. This specific image dimension was required by MitoSegNet. Adhering to this uniform image size across all tested systems ensured that the results were directly comparable. For Ilastik, we followed the guidelines of images segmentation and we annotated 10 images from different cell lines and imaging conditions to train the model before using it for the testing phase. In terms of accuracy, MitoSkel achieved a mean accuracy of approximately (0.951), indicative of its effectiveness in delineating mitochondria within microscopy images. MitoSegNet closely followed with a mean accuracy of approximately (0.926), while Ilastik exhibited a mean accuracy of about

(0.922). Regarding the F1 score, MitoSkel demonstrated the highest mean F1 score, approximately (0.762), which assesses balance between precision and recall. Ilastik provided a mean F1 score of about (0. 696), while MitoSegNet obtained a lower mean F1 score of approximately (0.620). Analysis of IoU, which measures the ability to capture the spatial extension of mitochondria, provided the highest mean IoU for MitoSkel, at (0.633). Ilastik obtained a mean IoU of about (0.553), while again MitoSegNet exhibited the lowest mean IoU, approximately (0.459). The specificity analysis revealed that our system achieved a mean specificity of approximately (0.974), demonstrating its capability to accurately identify true negative cases. MitoSegNet also demonstrated strong performance with a competitive mean specificity of around (0.971). In contrast, Ilastik showed a slightly lower mean specificity of approximately (0.932). Precision measurements further supported these findings, with MitoSkel exhibiting the highest mean precision at approximately (0.774), in line with its effectiveness in minimizing false positive outcomes. MitoSegNet closely followed with a mean precision of about (0.758). While Ilastik presented respectable precision, it reported a lower mean precision of approximately (0.621). Additionally, the analysis of Mean Absolute Error (MAE) showcased MitoSkel's performance with the lowest mean MAE of about 0.049, indicating strong alignment with ground truth annotations. In contrast, both MitoSegNet and Ilastik reported slightly higher mean MAE values,

Table 8Evaluation of the segmentation efficacy of MitoSkel is conducted alongside two other tools for mitochondria segmentation based on DL: Ilastik and MitoSegNet.

Model	F1Score	Accuracy	IoU	Precision	Specificity
MitoSkel	0.762	0. 951	0. 633	0. 774	0. 974
Ilastik	0.696	0.922	0.552	0.620	0.932
MitoSegNet	0.619	0.926	0. 458	0. 758	0. 971

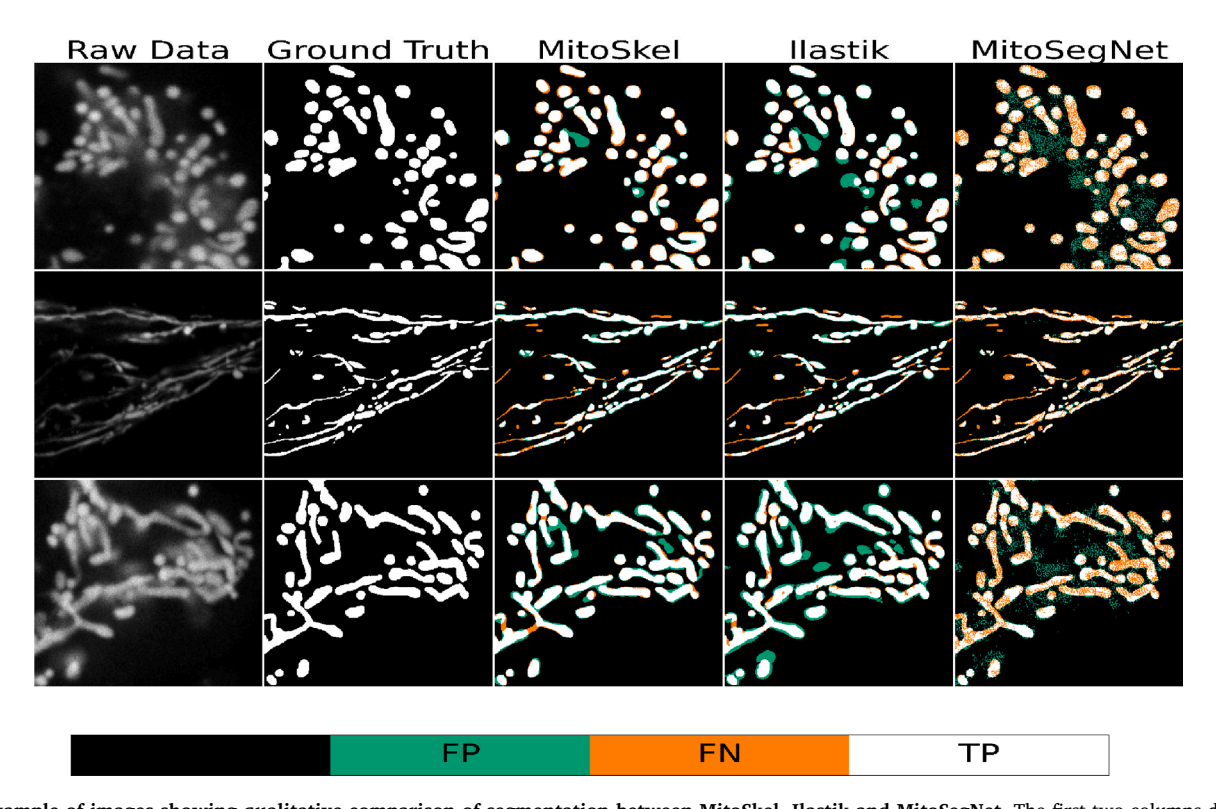


Fig. 3. Example of images showing qualitative comparison of segmentation between MitoSkel, Ilastik and MitoSegNet. The first two columns display the original images and their corresponding GT masks. The subsequent three columns illustrate the overlay between the ground truth mask and the generated segmentation masks for MitoSkel, Ilastik, and MitoSegNet, respectively. The color scheme used for the overlay depicts different segmentation outcomes: black represents true negatives (TN), green indicates false positives (FP), orange corresponds to false negatives (FN), and white true positives(TP). (For interpretation of the references to color in this figure legend, the reader is referred to the web version of this article.)

approximately (0.073) and (0.077), respectively Fig. 3 and Table 8. Collectively, these results show the effectiveness and reliability of MitoSkel for mitochondria segmentation in microscopy imaging applications.

3.3. Assessing segmentation performance on multiple cell lines

To assess the general applicability of MitoSkel, we conducted tests using four cell lines commonly used in mitochondria research: HeLa, HCT, U2OS and COS7. We manually annotated 8 images from each of the selected cell lines and applied data augmentation techniques to expand our dataset, resulting in 40 test images after five different geometric modifications. We then analysed the images with MitoSkel, Ilastik and MitoSegNet. In the context of Hela cells, MitoSkel achieved an accuracy of (0.947), closely trailing behind Ilastik at (0.951) but outperforming MitoSegNet (0.934), Furthermore, MitoSkel provided a F1 score of (0.787) slightly behind Ilastik (0.821), but above MitoSegNet (0.7099). The IoU of MitoSkel (0.650) illustrated a moderate overlap between the segmented regions and the ground truth while Ilastik attained a slightly higher IoU (0.698). With U2OS cells, MitoSkel's accuracy (0.954) was better than that of Ilastik (0.944) and on par with MitoSegNet (0.955). MitoSkel's F1 score reached (0.675), exceeding both Ilastik (0.644) and MitoSegNet (0.618). The IoU score of (0.556) also outperformed Ilastik (0.514) and MitoSegNet (0.486). In the case of HCT cells, MitoSkel provided the highest accuracy at (0.956), compared to Ilastik (0.937) and MitoSegNet (0.941). Its F1 score of (0.623) surpassed both Ilastik (0.527) and MitoSegNet (0.508). Moreover, the IoU of (0.458) depicted a robust alignment between MitoSkel's segmented regions and the ground truth, improving the performance of Ilastik (0.364) and MitoSegNet (0.342). Regarding COS7 cells, MitoSkel obtained better scores than the other two systems, with an accuracy of

0.965, followed by Ilastik (0.944) and MitoSegNet (0.923), a mean F1 score of 0.815, surpassing Ilastik (0.743) and MitoSegNet (0.526) and an improved IoU of (0.688), compared to Ilastik (0.592) and MitoSegNet (0.425) Fig. 4 and Table 9. In summary, MitoSkel consistently demonstrated significant performance in mitochondria segmentation across a diverse array of cell lines. While MitoSkel performed consistently well across most cell lines, its accuracy in HeLa cells was slightly lower than that of Ilastik. This difference can be attributed to the unique challenges posed by HeLa cells, which are characterized by a relatively high density of mitochondria and significant overlap between mitochondrial structures. These factors make precise segmentation more difficult, especially in distinguishing individual mitochondria. Ilastik, which incorporates manual feature-based classification, may have an advantage in handling such datasets by leveraging user-defined features tailored to the specific imaging conditions. In contrast, MitoSkel relies on automated feature learning, which, while offering a general and robust solution, may be less effective in specific challenging scenarios like dense mitochondrial networks in HeLa cells.

3.4. Assessing MitoSkel performance across diverse microscopy techniques

We also tested our MitoSkel segmentation tool across different microscopy techniques, namely Airyscan, SIM (Structured Illumination Microscopy), and confocal microscopy, and compared it with MitoSegNet and Ilastik. For Airyscan microscopy, MitoSkel achieved an accuracy of approximately 0. 971, better than MitoSegNet, (0.934), and Ilastik, (0.951). The F1 score for MitoSkel was 0.767, exceeding MitoSegNet (0.709) and Ilastik (0.746) and the IoU was (0.627), again improved compared to MitoSegNet (0.552) and Ilastik (0.5806). In the context of SIM microscopy, MitoSkel provided an accuracy score of 0.973,

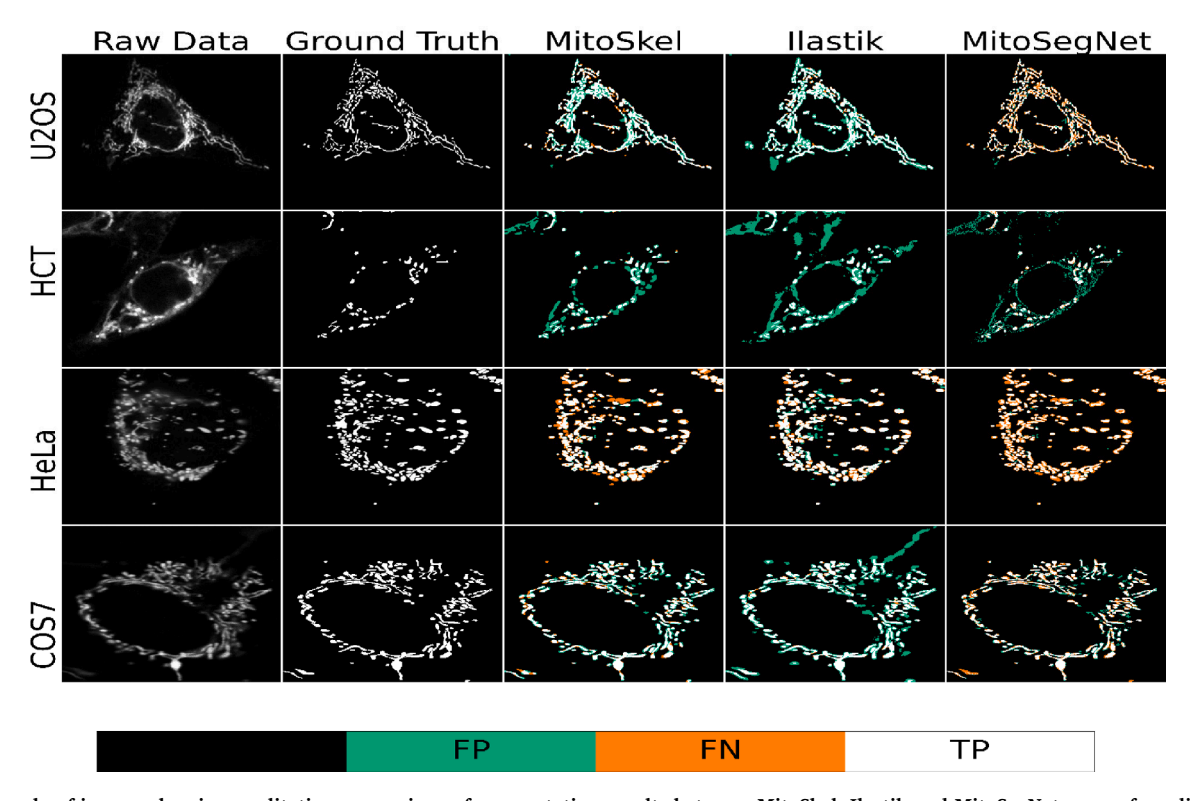


Fig. 4. Example of images showing qualitative comparison of segmentation results between MitoSkel, Ilastik and MitoSegNet across four different cell lines (U2OS, HCT, HeLa and COS7). The first two columns display the original images and their corresponding ground truth masks. The subsequent three columns illustrate the overlay between the ground truth mask and the generated segmentation masks for MitoSkel, Ilastik, and MitoSegNet, respectively. The color scheme used for the overlay depicts different segmentation outcomes: black represents true negatives (TN), green indicates false positives (FP), orange corresponds to false negatives (FN), and white signifies true positives (TP). (For interpretation of the references to color in this figure legend, the reader is referred to the web version of this article.)

Table 9Quantitative comparison of segmentation result across multiple cell lines: evaluation of the performance of our mitochondria segmentation system, MitoSkel, across various cell lines, comparing it with two established segmentation systems, Ilastik and MitoSegNet.

Cells	System	F1	Accuracy	IoU	Precision	Specificity
	MitoSkel	0.675	0.954	0.556	0.629	0.970
U2OS	Ilastik	0.644	0.944	0.513	0.554	0.955
	MitoSegNet	0.618	0.955	0.486	0.712	0.984
	MitoSkel	0.787	0.947	0.650	0.954	0.994
HeLa	Ilastik	0.821	0.951	0.698	0.865	0.979
	MitoSegNet	0.709	0.934	0.552	0.964	0.996
	MitoSkel	0.623	0.956	0.458	0.495	0.958
HCT	Ilastik	0.527	0.937	0.364	0.379	0.939
	MitoSegNet	0.508	0.941	0.342	0.387	0.950
	MitoSkel	0.8155	0.965	0.688	0.752	0.972
COS7	Ilastik	0.743	0.944	0.592	0.605	0.942
	MitoSegNet	0.526	0.923	0.425	0.548	0.961

exceeding both MitoSegNet, (0.946), and Ilastik (0.946). The F1 score for MitoSkel was 0.889, whereas MitoSegNet (0.795) and Ilastik (0.714) lagged behind. However, the IoU score for MitoSkel was comparatively lower (0.494) compared to MitoSegNet (0.5368) and Ilastik (0.565). This suggests that while MitoSkel excels in terms of accuracy, there may be slight challenges in delineating mitochondrial structures accurately according to the IoU metric when using SIM microscopy. With Confocal microscopy, MitoSkel's accuracy (0.951) was comparable to Ilastik (0.951), followed by MitoSegNet (0.941). The F1 score for MitoSkel was (0.761), surpassing MitoSegNet (0.706) but slightly below Ilastik (0.785). The IoU score was moderate at (0.534), while Ilastik (0.650) demonstrated a slightly higher IoU score Fig. 5 and Table 10. In conclusion, MitoSkel demonstrated high level of accuracy in Airyscan microscopy, while maintaining robust performance in SIM and confocal microscopy as well. Our evaluation shows that MitoSkel is a versatile and effective system for mitochondria segmentation across various microscopy techniques.

The performance of MitoSkel under different microscopy techniques is influenced by the inherent noise and data variance present in each method. Airyscan and SIM microscopy, which offers high-resolution images with minimal noise, supports MitoSkel's strong performance. For confocal microscopy, the moderate resolution and higher noise levels may contribute to the observed lower F1 and IoU scores compared to Airyscan and SIM. These findings illustrate that variations in resolution, contrast, and noise across microscopy techniques have a tangible impact on segmentation performance. Future refinements to MitoSkel could focus on improving robustness to structured illumination artifacts and noise through advanced preprocessing or model training strategies.

3.5. Methodology for Calculating mitochondrial structural metrics

To comprehensively understand mitochondrial dynamics and their

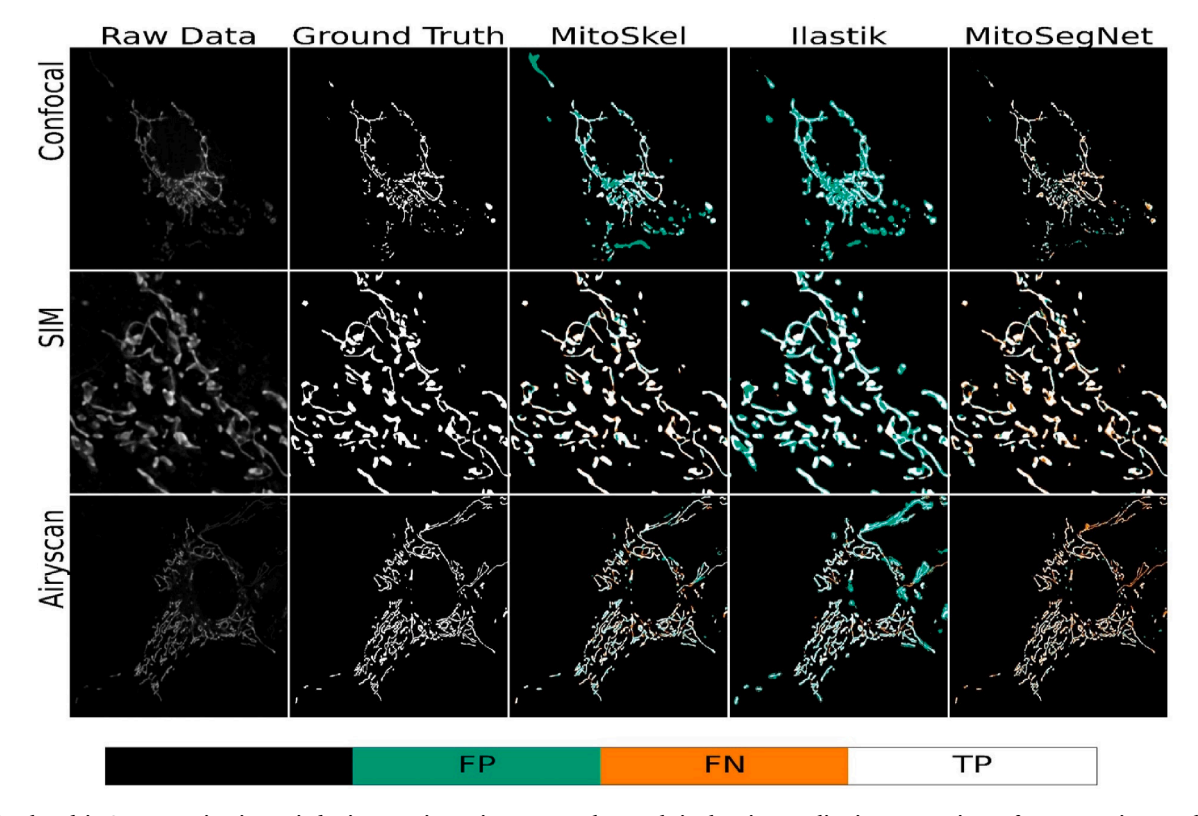


Fig. 5. Mitochondria Segmentation in Varied Microscopic Environments: the result is showing qualitative comparison of segmentation results between MitoSkel, Ilastik and MitoSegNet across different microscopes: Confocal, SIM and Airyscan. The first two columns display the original images and their corresponding ground truth masks. The subsequent three columns illustrate the overlay between the ground truth mask and the generated segmentation masks for MitoSkel, Ilastik, and MitoSegNet, respectively.

Table 10

Quantitative Evaluation of Segmentation Metrics Across Different Microscopy Systems:a comparison between our proposed system MitoSkel and mitochondria DL based segmentation systems: Ilastik and MitoSegNet.

Microscope	System	F1	Accuracy	IoU	Precision	Specificity
	MitoSkel	0.761	0.951	0.629	0.866	0.987
Confocal	Ilastik	0.775	0.951	0.650	0.783	0.973
	MitoSegNet	0.686	0.941	0.534	0.890	0.991
	MitoSkel	0.889	0.973	0.802	0.892	0.985
SIM	Ilastik	0.795	0.946	0.661	0.720	0.953
	MitoSegNet	0.656	0.940	0.494	0.972	0.997
Airyscan	MitoSkel	0.776	0.973	0.635	0.810	0.988
	Ilastik	0.722	0.961	0.568	0.628	0.967
	MitoSegNet	0.763	0.974	0.619	0.880	0.994

role in cellular function, accurately quantifying morphological characteristics is essential. To quantify key parameters of mitochondria, we developed an image analysis approach to extract and measure perimeter, area, thickness, circularity, and total branch length from segmented images.

Perimeter and Area: The perimeter was measured as the total distance around the boundary of each mitochondrial structure, while the area represented the total number of pixels within the contour. These metrics provide insight into the size and boundary complexity of the mitochondria. The perimeter P can be calculated using:

$$P = \sum_{i=1}^{N} d_i \tag{5}$$

Where d_i is the distance between consecutive points along the contour of the object, and N is the total number of the points on the contour.

The area A can be defined as the sum of all pixels enclosed by the contour:

$$A = \sum_{(x,y) \in Contour} 1 \tag{6}$$

Where (x,y) are the coordinates of pixels within the boundary of the mitochondrial structure.

Circularity: Circularity was calculated to assess the shape of the

mitochondria, with a value closer to 1 indicating a more circular structure. Circularity C is calculated by:

$$C = \frac{4\pi A}{P^2} \tag{7}$$

This equation provides a measure of how close the shape is to a perfect circle, with C=1 indicating a perfect circle.

Thickness: The thickness of each mitochondrial branch was evaluated by analyzing the skeletonized representation of the structure. The mean thickness was determined by averaging the width across the branches, providing a measure of the overall diameter of mitochondrial segments. The average thickness T of mitochondrial branches can be estimated using:

$$T = \frac{2 \times \sum_{i=1}^{M} t_i}{M} \tag{8}$$

where t_i represents the local thickness at each skeleton pixel and M is the total number of pixels along the skeleton.

Total Branch Length: The total branch length was calculated by summing the lengths of all individual branches within each mitochondrial structure, allowing for the evaluation of network complexity and connectivity. More details on how we calculated the parameters are shown in Fig. 6.

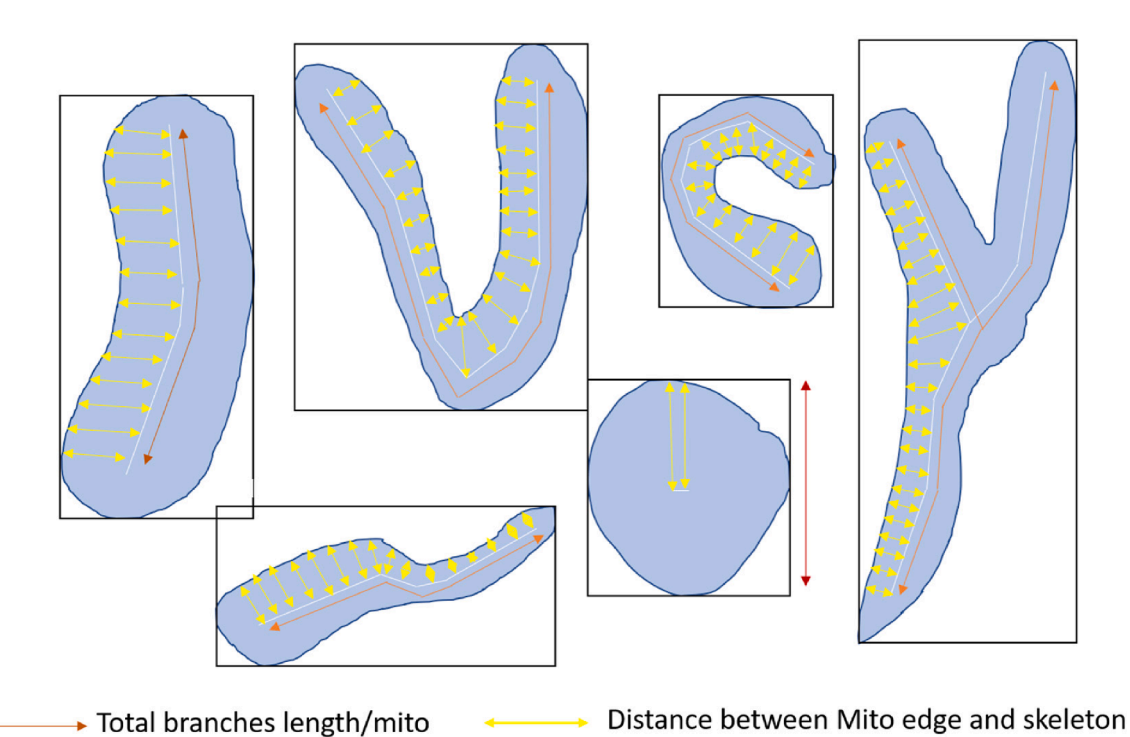


Fig. 6. Schematic Representation of Morphometric Parameter Calculation.

3.6. Benchmarking the skeletonization performance of MitoSkel

Skeletonization is a useful approach towards the quantification of mitochondrial properties. It transforms the complex network of mitochondria into a simplified, skeleton-like framework from which information about branching patterns, interconnections, and spatial organization of mitochondria within cells can be extracted [5,34]. To this end, we incorporated a skeletonization tool in MitoSkel, which we also benchmarked against those of MitoSegNet and Ilastik. We used a diverse dataset comprising 40 images sourced from various cell lines and microscopes (see Methods and materials). Images underwent segmentation processing, resulting in binary masks that were subsequently skeletonized with the different tools. Our comparison also included a comparison with MINA [5], a recognized system for mitochondria skeletonization. We considered several metrics, including total numbers of branches, total lengths, and mean branch lengths.

The average branch length for the ground truth stood at 3.515 $\mu m,$ closely aligned with MitoSkel average branch length of 3.219 $\mu m.$ In contrast, Ilastik and MitoSegNet provided average branch lengths of 2.507 μm and 2.002 μm respectively, both farther from the ground truth

0

GT

Mitoskel Mitosegnet

Fig. 7B. Interpreting the average total branches provides insights into the performance of each segmentation system in representing the branching structure of mitochondria on average across the dataset. The ground truth average of 238.809 branches serves as the reference point for our data sate. MitoSkel's average total branches number of 207.261 suggests a slightly lower count compared to the ground truth average. In contrast, Ilastik's average total branches number of 416.952 indicates a tendency to overestimate the branching structure on average. Mito-SegNet's average total branches number of 720.023 substantially deviates from the ground truth average Fig. 7C. The analysis of the total length of mitochondrial branches also provides a valuable measure of the performance of each segmentation system. The ground truth of the testing data exhibited a total length of branches of 758.200 µm. MitoSkel achieved remarkable accuracy, with a total length of branches of 620.485 µm. In contrast, MitoSegNet exhibits a substantial overestimation, recording a total length of branches of 1285.660 µm. Similarly, Ilastik shows a moderate overestimation with a total length of branches of 959.256 µm, indicating that both systems tend to capture more of the branching structure's length than actually present in the images Fig. 7A. In conclusion, the close alignment of MitoSkel analysis

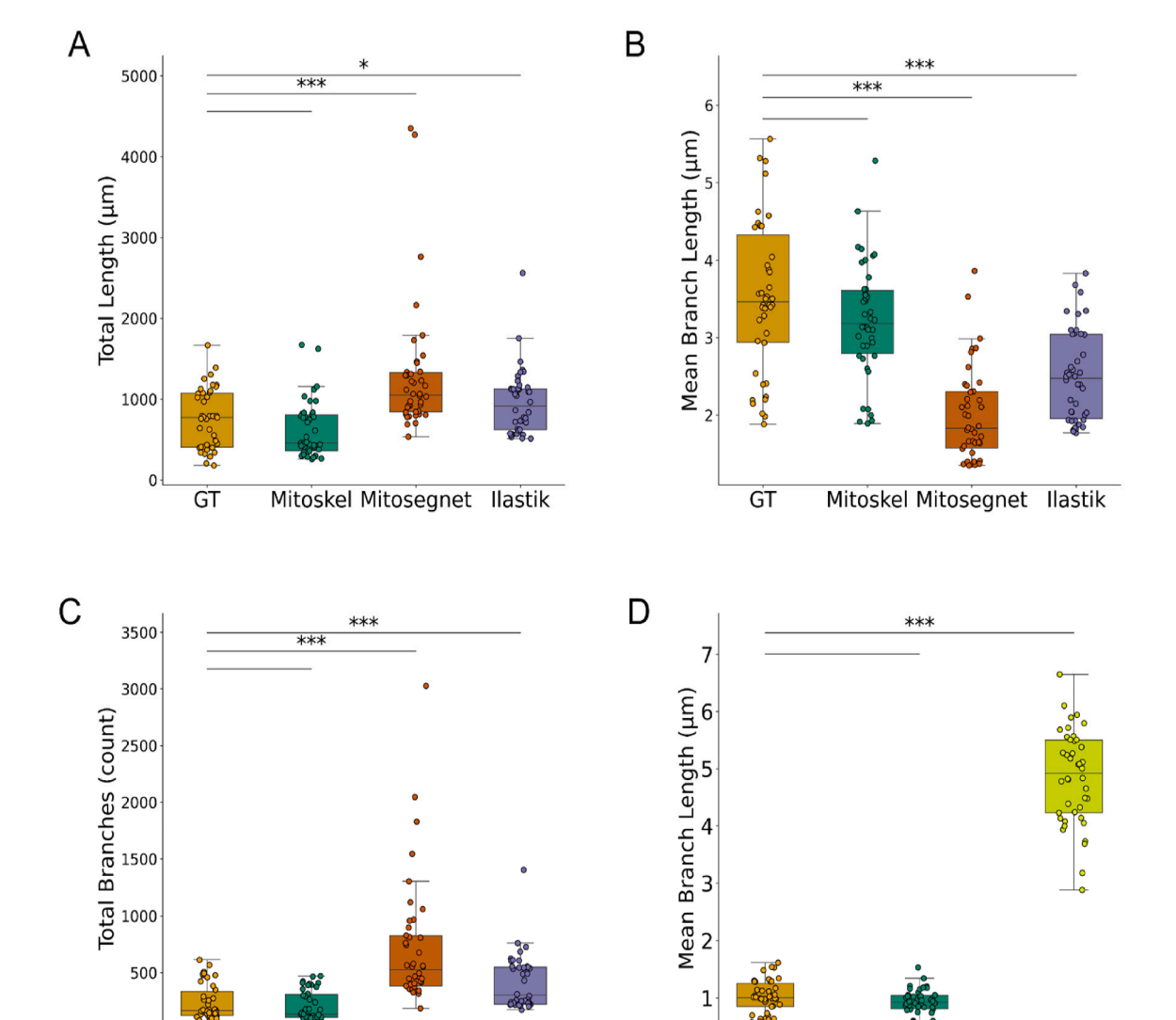


Fig. 7. MitoSkel skeletonization results and a skeletons comparison with MINA, Ilastik and MitoSegNet: A. show a comparison between MitoSkel, Ilastik and MitoSegNet in term of total length of the mitochondria network. B. shows a comparison between MitoSkel, Ilastik and MitoSegNet in terms of the mean branch length of mitochondria, C. shows a comparison between MitoSkel, Ilastik and MitoSegNet in terms of total number of branches and D. shows comparison between our proposed system MitoSkel and MINA skeletonization system in terms of mean branch lengths. 40 images were used in all the conditions.

GT

Mitoskel

MINA

llastik

with the ground truth in total branches number and total length of branches as well as the average length of mitochondria underscores its reliability and precision. Conversely, MitoSegNet tends to overestimate, while Ilastik demonstrates a moderate tendency to overestimate. The visual comparison between the overlapped areas of the skeleton and the binary mask revealed a high degree of accuracy and alignment Fig. 8A. This indicates that MitoSkel effectively captures the essential structure of the original image while maintaining its topological integrity, as shown by the substantial overlap observed in our analyses. When comparing the mitochondrial skeletonization results with those from the MINA system, a workflow for analyzing mitochondrial morphology using fluorescence images or 3D stacks, we observed notable differences in low and high-resolution images. In cases of low-resolution imaging, the skeletons by MitoSkel mapped accurately onto the mitochondrial structures, indicating a high level of precision in segmentation Fig. 8B and C. Conversely, the skeletonization produced by MINA failed to align accurately with the underlying raw images, suggesting that the system may not be adequately equipped to handle lower-resolution data. Under conditions of high-resolution, MINA showed an improvement in the skeletonization results close to Mitoskel high performance of accuracy and alignment Fig. 8D and E. However, the comparison of the mean branch length between MitoSkel, MINA, and the ground truth revealed significant variations Fig. 7D. For a ground truth mean branch length of 3.515 µm, Mina reported a considerably higher mean branch length of 16.722 µm, suggesting a substantial overestimation. This is in contrast with MitoSkel, which with 3.219 µm was closer to the ground truth,

indicating a relatively accurate representation of the mean branch length.

3.7. MitoSkel Graphical user interface

In addition to its robust segmentation capabilities, MitoSkel offers a user-friendly interface designed to streamline the process of mitochondrial analysis for researchers. Its intuitive design and user-friendly features simplify the segmentation and quantification process, making it accessible to users with varying levels of expertise in image analysis. MitoSkel is versatile, handling different image sizes effectively. Users can select an image size closest to their input images for optimal convenience or opt for a larger size to potentially enhance segmentation results. A screenshot of the graphical user interface is shown in Figs. 9 and 10. Furthermore, MitoSkel provides a wide range of data outputs, catering to diverse research needs. Researchers can obtain comprehensive metrics such as branch lengths, thickness, circularity, area, and perimeter, which offer valuable insights into mitochondrial morphology and structure.

Additionally, detailed skeletonization results including branch number, lengths, and connectivity are provided, enabling researchers to dissect the spatial organization and complexity of mitochondrial networks. More details are provided in the screenshots in Figs. 11 and 12 To facilitate data management and subsequent analysis, all these parameters are collated into an Excel file, ensuring ease of access and compatibility with common analysis tools. This comprehensive suite of

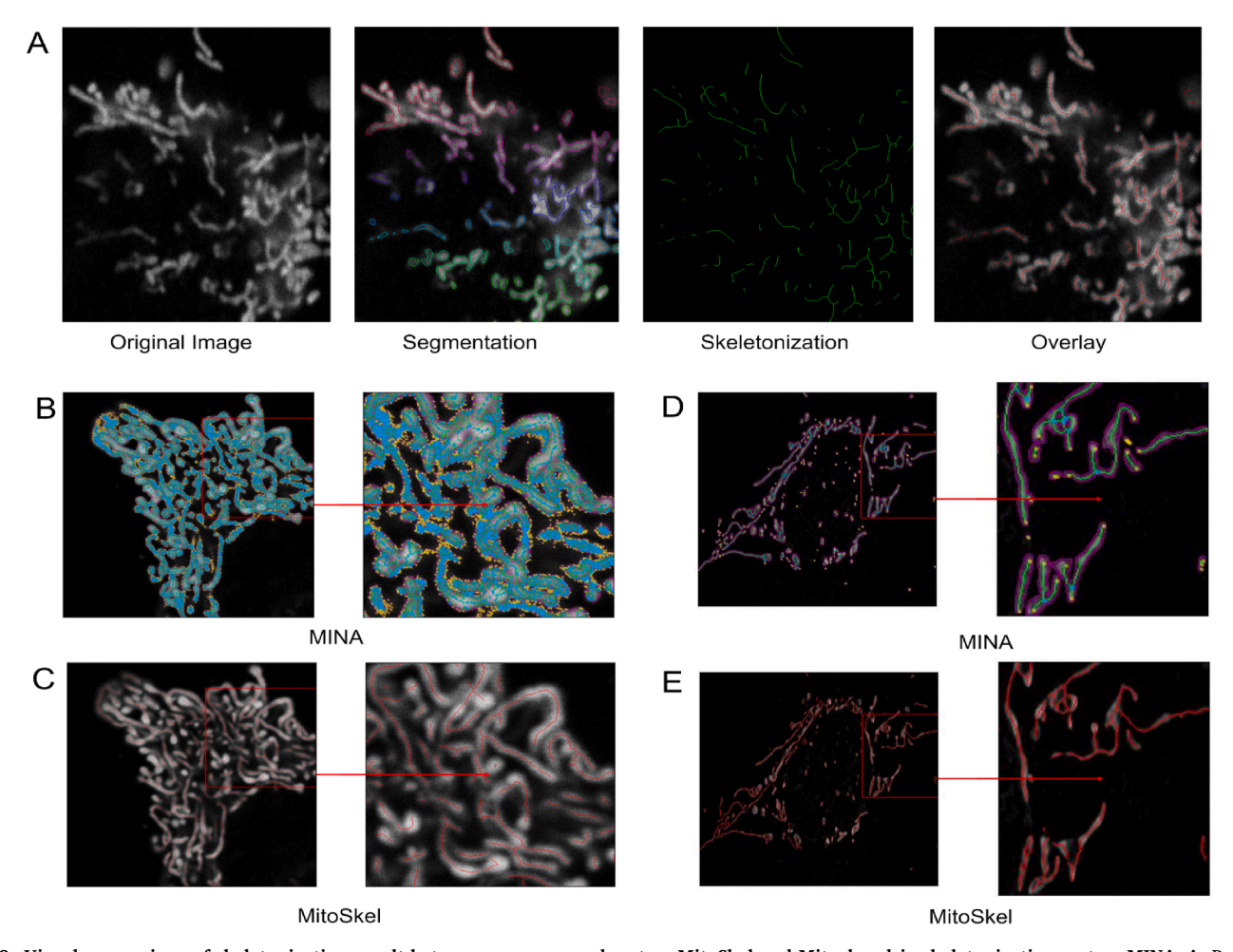


Fig. 8. Visual comparison of skeletonization result between our proposed system MitoSkel and Mitochondria skeletonization system MINA. A. Presents MitoSkel skeletonization result: the first column presents the initial image, then the segmentation contours followed by the skeletonization result and finally the overlay between the original data and the skeleton. B. illustrate the skeleton result of MINA tool in low resolution imaging. C. present the skeleton result of MitoSkel in low resolution. D. shows the MINA skeletonization result in high resolution. E. displays the MitoSkel result in high resolution condition.

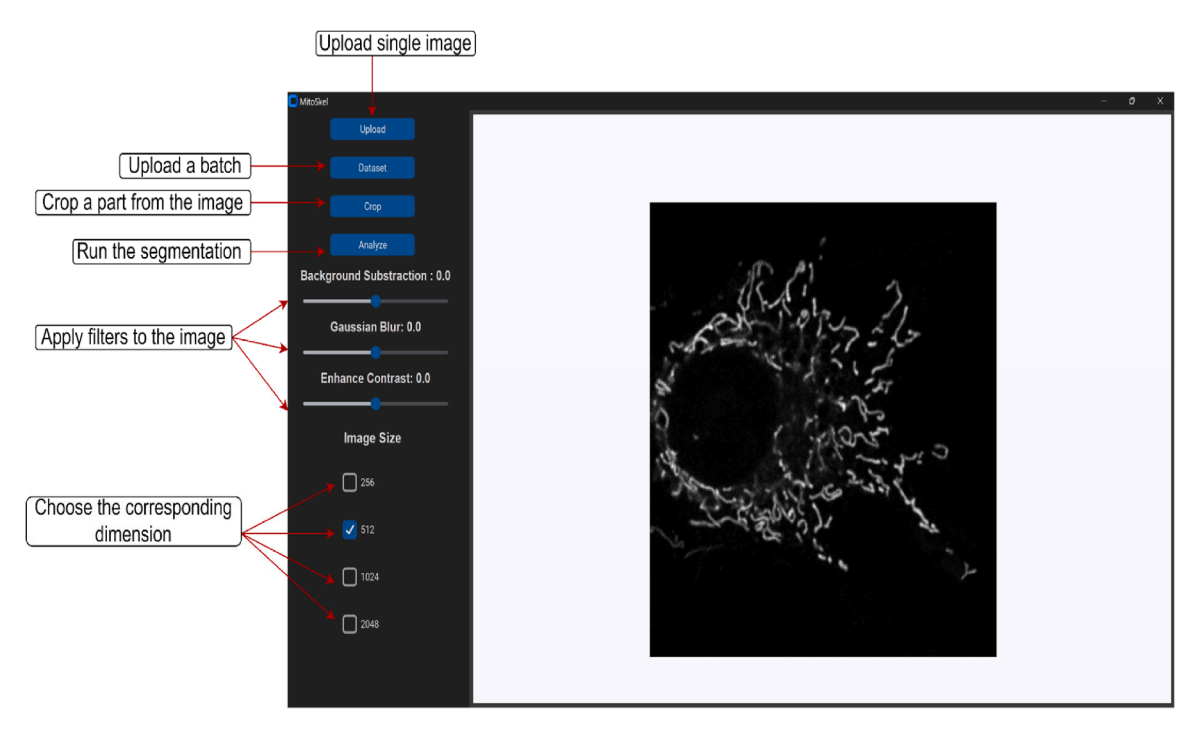


Fig. 9. MitoSkel Graphical User Interface: A user-friendly interface is used to analyse mitochondria morphology. The interface provides buttons to analyse individual as well as batches of images. Background subtraction, contrast enhancement, and Gaussian filters can be applied to the original image to enhance the quality of the segmentation results. A checkbox is provided to select the adequate image size.

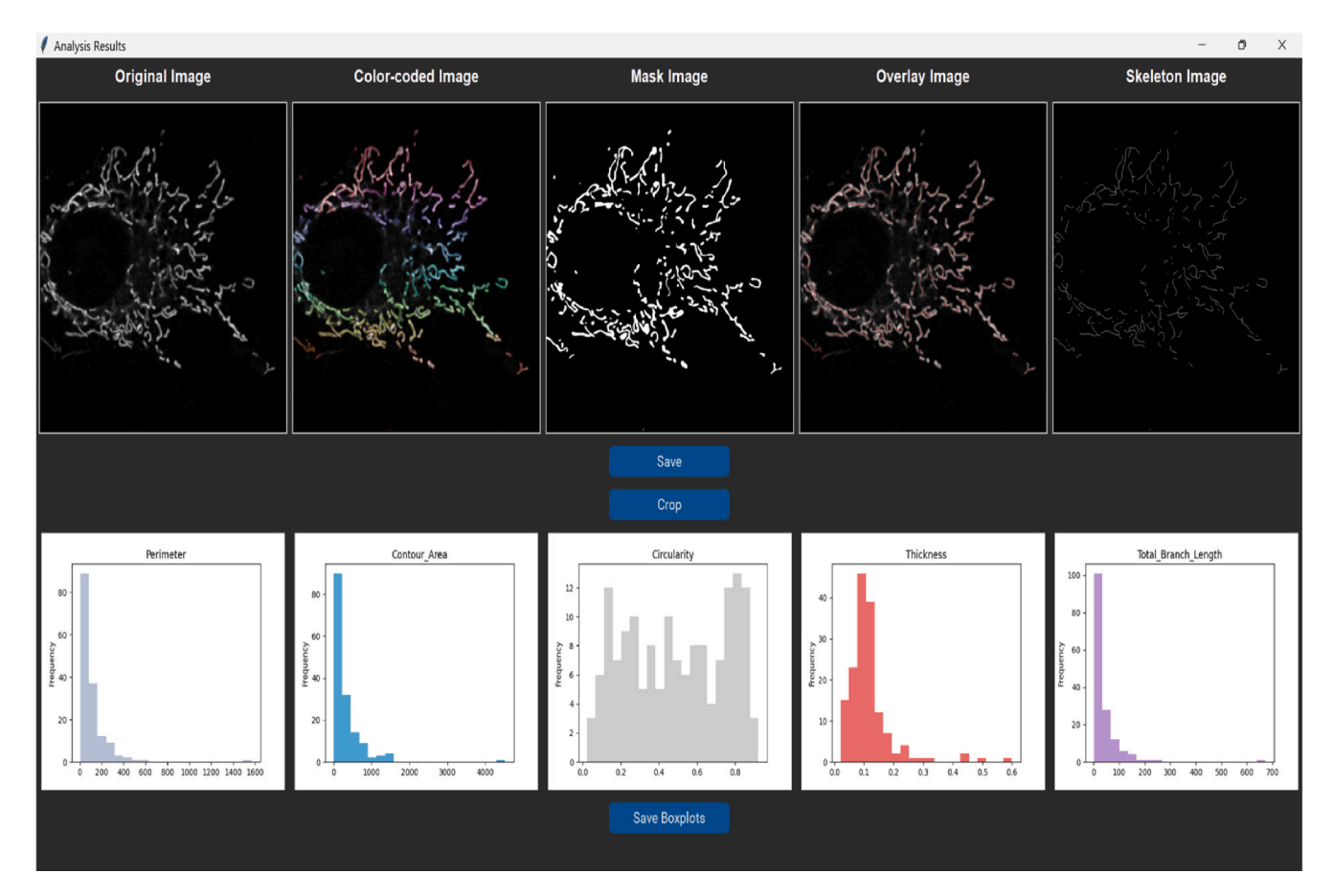


Fig. 10. Output of MitoSkel Graphical User Interface. Examples of segmentation and skeletonization result are shown. Buttons for saving the histograms, segmentation data, and the generated skeletons excels files are available.

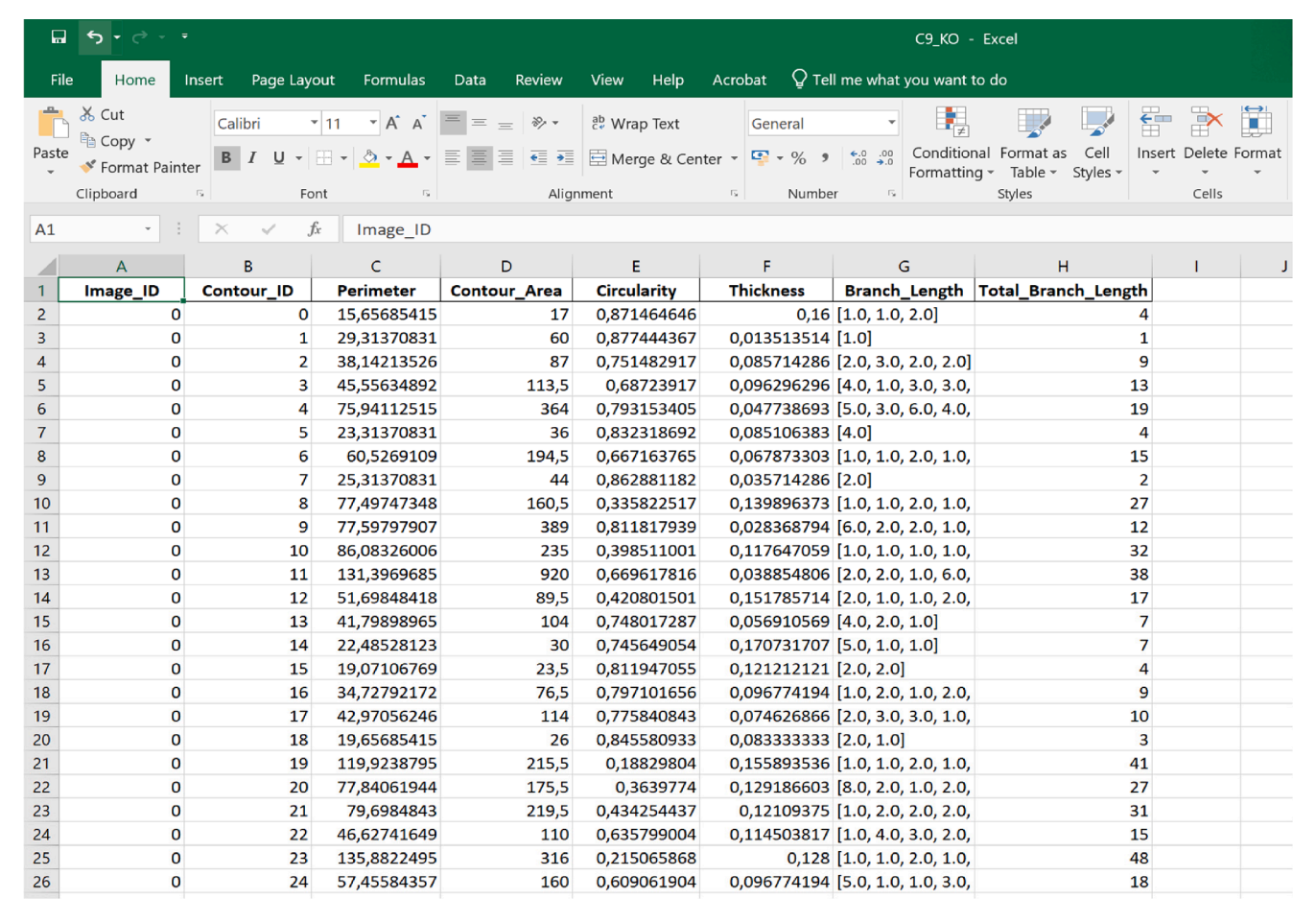


Fig. 11. Excel file for Connectivity and Structural Parameters of Skeletonized Networks.

features makes MitoSkel an efficient tool for mitochondrial analysis, allowing researchers to uncover new insights into mitochondrial biology.

3.8. Assessing mitochondrial morphology Changes in HeLa cells upon DRP1 depletion and CCCP Exposure

Next, we evaluated the segmentation and quantification of the properties of the mitochondrial network using samples under different morphological states, concretely, normal, fragmented, and elongated. As example of elongated mitochondria, we used HeLa cells with a knockout (KO) of Dynamin-related protein 1 (Drp1) Fig. 13C. Drp1 is an essential regulator of mitochondrial fission and its absence leads to elongation of mitochondria [35–37]. We used treatment of wild type HeLa cells with carbonyl cyanide m-chlorophenyl hydrazone (CCCP) to generate samples with fragmented mitochondria Fig. 13A. CCCP is a mitochondrial uncoupling agent that disrupts mitochondrial membrane potential and promotes fragmentation [38]. Untreated wild type HeLa cells were used as a reference sample for a "normal" mitochondrial network Fig. 13B.

Importantly, analysis of the images acquired for the three mitochondrial reference states with MitoSkel allowed us to identify and quantify distinct morphological changes. The average branch length from the skeletonization results post-segmentation revealed significant elongation in Drp1-depleted cells with 5.952 μm , compared to 2.54 μm in CCCP-treated cells and 3.216 μm in the wild-type. In terms of average thickness, Drp1 KO cells exhibited a value of 0.1116 μm , indicative of slender mitochondrial profiles when compared to CCCP-treated cells at 0.0730 μm and wild-type at 0.0920 μm . In line with this, the average percentage of circularity measure inversely related to the elongation of

mitochondrion was lowest in Drp1-depleted cells (52.13 %) and wild-type cells (61.56 %). In contrast, CCCP-treated cells exhibited the highest circularity (69.43 %), reflecting a more fragmented phenotype. Fig. 14A-D. These quantitative results by MitoSkel accurately reflect the expected morphological characteristics, thereby validating the system's efficacy in distinguishing and quantifying variations in mitochondrial structure under varying physiological states.

4. Discussion

In our study, we addressed current challenges in mitochondrial segmentation in the analysis of 2D images, characterized by complex issues such as mitochondrial overlap, variability in image acquisition, and the diverse morphologies exhibited by mitochondria across different cell lines. Prior work in mitochondrial segmentation and quantification has often been hampered, especially when dealing with the dual challenges of image noise and low resolution, by the varied mitochondrial morphologies observed across cell types. MitoSkel represents a significant improvement in overcoming these barriers.

A cornerstone of our approach is the diversity of the image data used for training, which encompasses a wide range of microscopy modes and cell lines. This diverse dataset has been instrumental in enhancing the generalizability of our mode, enabling it to adeptly segment mitochondria across a multitude of imaging conditions and cell types.

In addition, the adoption of an advanced deep learning model, GAU-Net, a version of U-Net augmented with an attention thresholding mechanism and the integration of a Gabor layer into the original model, has proven critical. The Gabor filter's effectiveness in feature detection across multiple scales stems from its unique ability to capture both fine details and broader patterns simultaneously. This property is

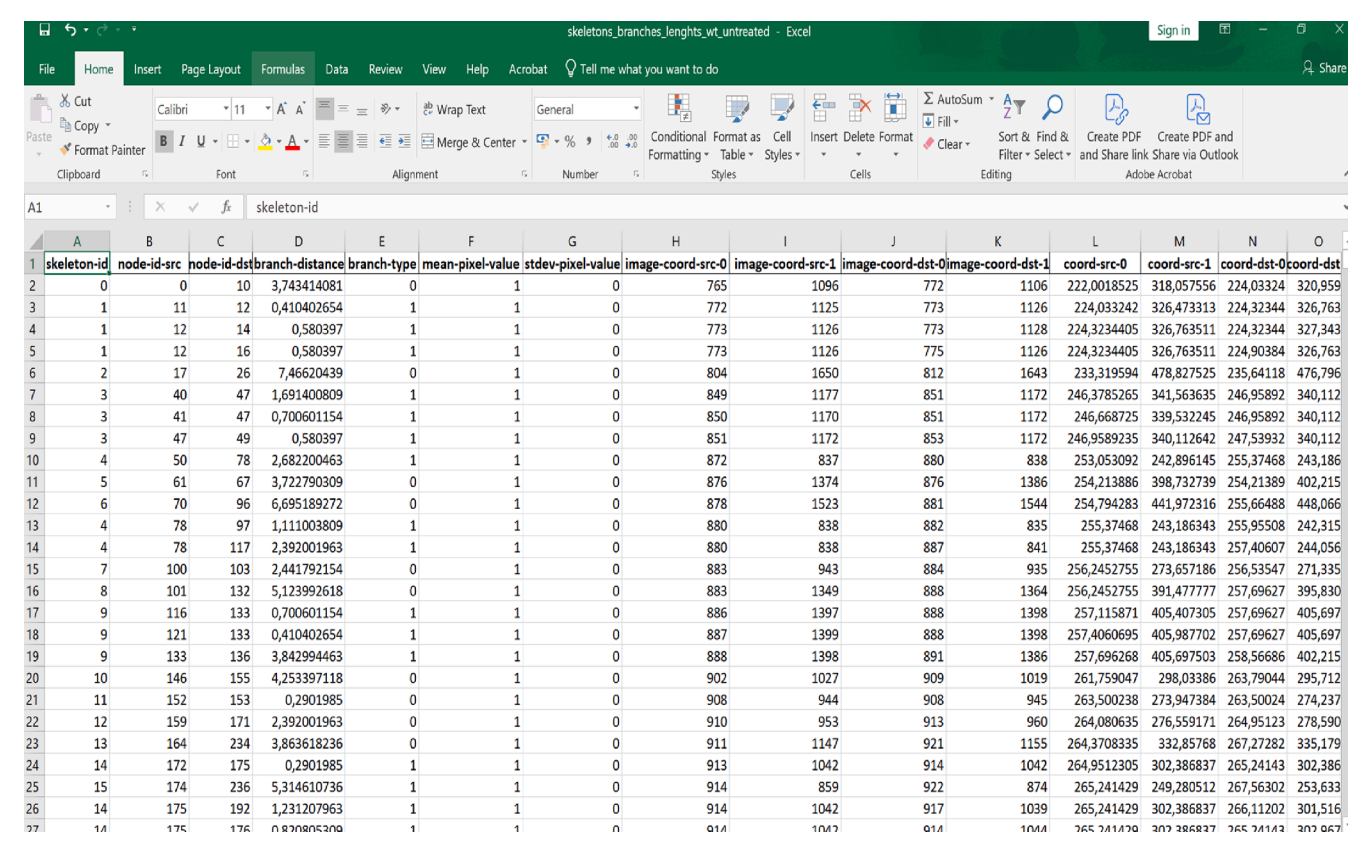


Fig. 12. Excel file for Morphometric Analysis of Segmented Mitochondria: Perimeter, Area, Thickness, Circularity, and Total Branch Length.

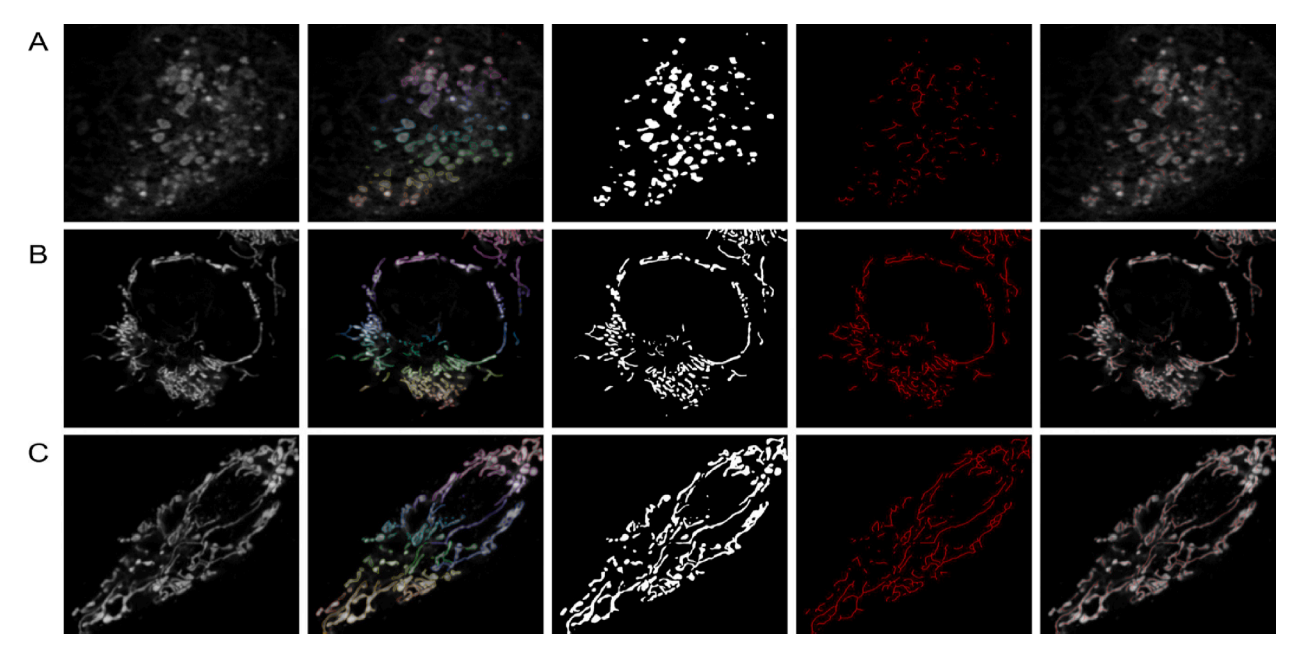


Fig. 13. Mitochondrial Morphology Changes in HeLa Cells DRP1 KO and upon CCCP Exposure. A. An example of a HeLa cell treated with CCCP, displaying fragmented morphology. B. An example image of a wild-type cell with normal morphology. C. HeLa DRP1 KO cell exhibiting elongated mitochondrial morphology. Each row presents, respectively, the initial image, segmentation result, detected mask, skeleton result, and overlay of the skeleton with the initial image.

particularly advantageous when dealing with the diverse shapes and structures of mitochondria, which can vary significantly in size and morphology across different cellular contexts. By leveraging the Gabor filter's adaptability, our model can efficiently extract relevant features from mitochondria at various scales, enabling it to discern subtle nuances in mitochondrial morphology. Moreover, the integration of the

attention thresholding mechanism adds another layer of sophistication to our approach. By selectively focusing the model's attention on regions of interest within the image, such as mitochondria, while minimizing distractions from background noise, we can effectively guide the learning process towards key features of biological significance. We expect GAU-Net to prove a valuable innovation for the improvement of a

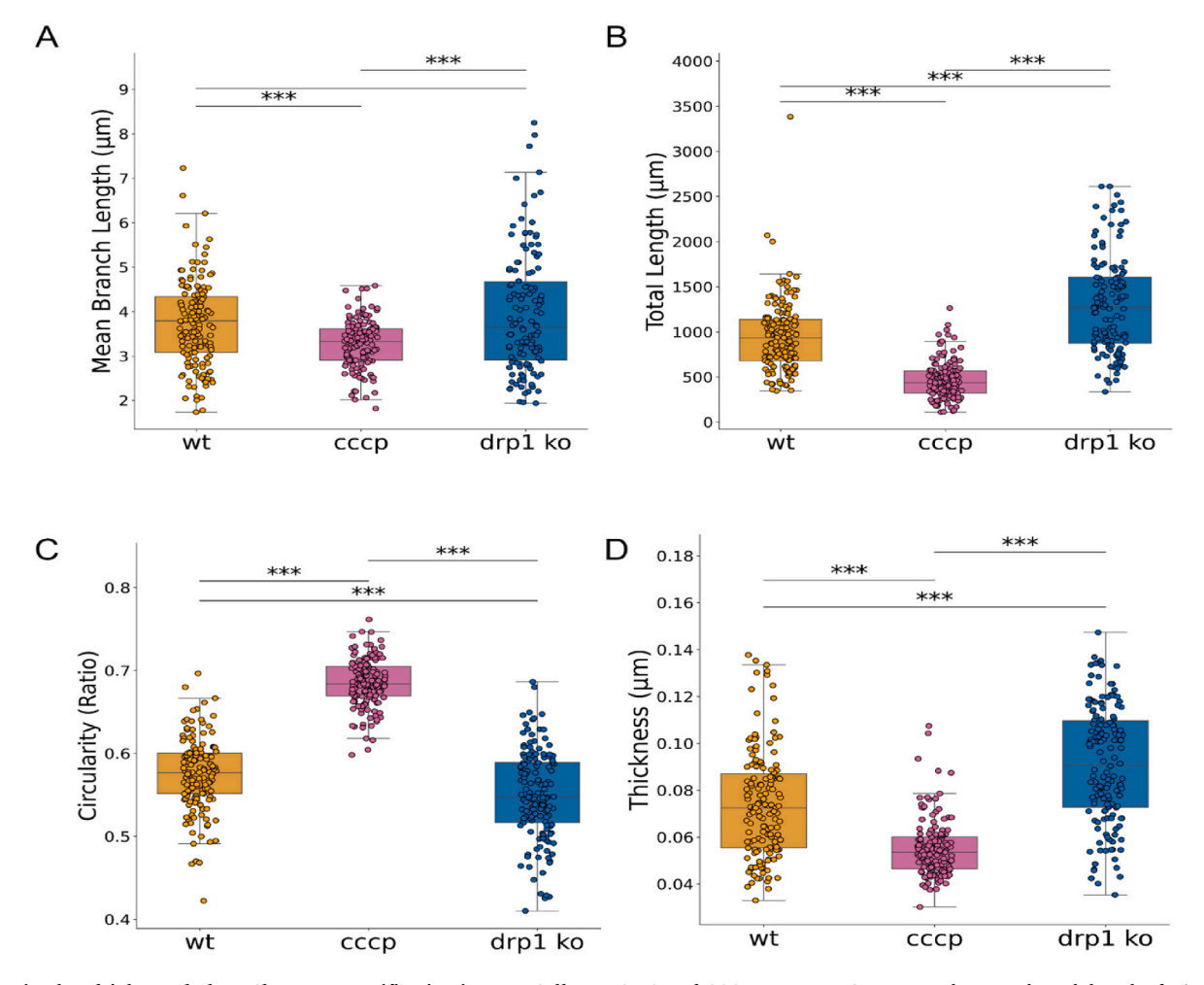


Fig. 14. Mitochondrial Morphology Changes quantification in HeLa Cells DRP1 KO and CCCP Exposure: A. presents the Mean branch length of mitochondria skeletons in the three conditions: wt, cccp and drp1. B. comparison of the total length of the mitochondria network. C. displays a comparison of the circularity ratio of mitochondria. D. presents the thickness of mitochondria in the same condition.

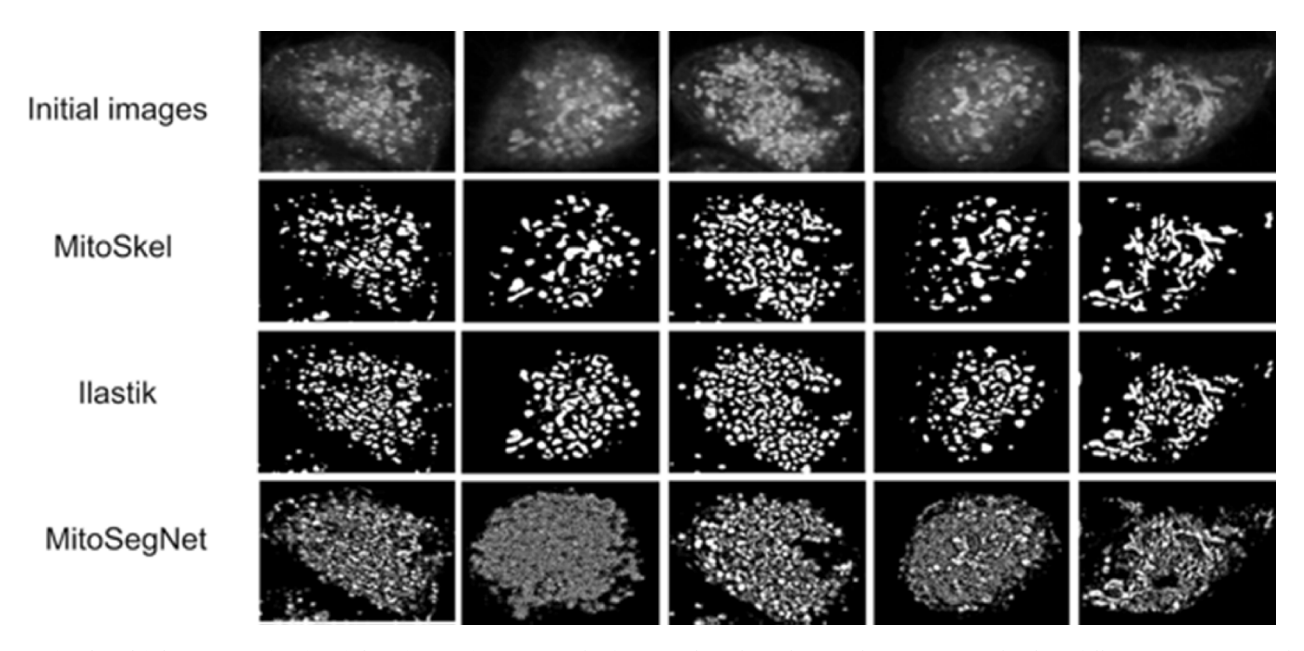


Fig. 15. Mitochondrial Segmentation in High-Noise Environments: the first-row data show the initial noisy images, the three following rows present the segmentation result of MitoSkel, Ilastik and MitoSegNet in noisy conditions.

diverse range of segmentation tasks from complex fluorescence microscopy images.

MitoSkel proficiently identifies mitochondrial areas, even in images that are significantly affected by noise or exhibit high levels of complexity. A comparative analysis with established systems such as MitoSegNet and Ilastik shows the improved performance of our system Fig. 15. This was particularly evident not only in the segmentation of lower quality images, but also in the skeletonization of the identified mitochondria, a key step in the quantitative parametrization of the mitochondrial network. MitoSkel does not necessitate human intervention or annotation prior to segmentation such as Ilastik. Moreover, our system not only provides segmentation results but also offers quantification of morphological shapes, reducing the time and resources required by biologists when analyzing mitochondrial shapes. Our system also addresses and resolves common constraints encountered in other segmentation tools, such as stringent requirements regarding image format or size. By enabling segmentation that conforms to the original dimensions of the images, our system assures enhanced accuracy and reliability in the results.

Evaluation of MitoSkel across different cell lines revealed subtle variations in performance. While MitoSkel performed equally with Ilastik in HeLa and U2OS cells, it was most effective in COS7 and HCT cells. These variations could be due to differences in staining quality, mitochondrial density, and cell morphology across cell lines. Specifically, the slightly lower accuracy observed in HeLa cells is likely due to the unique challenges posed by this cell line, including high mitochondrial density and significant structural overlap. These characteristics make distinguishing individual mitochondria particularly difficult for fully automated methods like MitoSkel. By contrast, Ilastik benefits from manual feature-based classification, allowing for tailored adjustments that improve segmentation in such challenging conditions. Despite this, MitoSkel's performance remains robust across a wide range of imaging conditions, achieving comparable results to Ilastik in confocal imaging, matching MitoSegNet in SIM images, and exceeding both in Airyscan conditions.

However, we recognize that our system is not without its limitations. A significant hurdle we encounter is the precise delineation of overlapping mitochondria, especially evident in low-resolution images where distinguishing individual mitochondria becomes notably challenging, even for the human eye. The complexity of their shapes further exacerbates this difficulty, leading to instances where users may struggle to annotate images accurately. Another limitation of our model is its slower training speed compared to the original U-Net. This decrease in performance speed is due to the integration of an additional Gabor layer and TAM. The Gabor layer, while beneficial for feature extraction, adds computational complexity which results in longer training times.

Furthermore, while our dataset includes images from multiple cell lines and microscopy techniques, it may not cover the full spectrum of experimental conditions, potentially limiting the generalizability of MitoSkel. Variations in staining protocols, imaging resolution, and mitochondrial morphology in other cell types or microscopy methods could impact performance. Lastly, our evaluation relied on manually annotated datasets, which may introduce variability in the ground truth. Future improvements could address these challenges by incorporating automated annotation methods, expanding the diversity of the training dataset, and optimizing the computational efficiency of MitoSkel to make it more accessible to researchers with limited computational resources.

In conclusion, we report here MitoSkel, a new AI-based platform with a user-friendly interface for the automatic segmentation of individual mitochondria and the quantification of their features from 2D fluorescence microscopy images. Our system can be applied to images obtained from different cell types and microscopy modes. Importantly, we show that MitoSkel can identify quantitative differences in the properties of distinct mitochondrial morphologies. By offering flexibility, precision, and user accessibility, MitoSkel system offers a useful

tool for researchers in cell biology and related disciplines, driving forward our understanding of mitochondrial dynamics and functionality.

5. Materials and methods

5.1. Dataset preparation and pre-processing

The ground truth annotations were created by a collaborative team comprising a biologist and two informaticians, employing the "Labelkit" AI tool for image annotation. This process involved manually annotating a portion of the image, followed by using Labelkit to generate the initial mask, with subsequent manual corrections to address any missing or inaccurate annotations. The training dataset for the GAU-Net model comprised 102 images, including 12 U2OS images captured with SIM, 67 U2OS confocal images, and 23 confocal images of HeLa cells. These images were divided into 512x512 patches and augmented using five modifications, resulting in a total of 1470 images. For the testing phase, we utilized 30 U2OS (confocal and SIM) images and 6 HeLa (confocal) images, which were also cropped into 512x512 patches and augmented similarly to the training dataset.

Cell-lines testing dataset: To assess the system's efficiency across different cell lines, we employed 8 images from each cell lines: U2OS, HCT, COS7, and HeLa cells, augmenting them accordingly to have 40 images per cell condition.

Microscopy testing dataset: To evaluate the proposed system under different microscopy imaging conditions, we utilized 8 images of U2OS cells (SIM), 8 images of primary LF cells (Airyscan), and 8 images of HeLa cells (confocal). All the images were augmented.

Skeleton testing dataset: To test the skeletonization performance, we used 40 images from different cell lines and conditions.

The ground truth of all the training and testing dataset were manually labelled using LabelKit as describing previously.

All data augmentation applied included rotations, horizontal and vertical flips, as well as scaling transformations to enhance variability and improve the model's generalization capabilities.

5.2. Cell culture

HeLa cells stably expressing Tom20-mEGFP, COS-7, and LF cells were cultured in DMEM[39] (4.5 g/L D-Glucose, Sodium Pyruvate, GlutaMAX; Gibco, Cat# 10569010). HCT cells were cultured in modified McCoy's 5A (GlutaMAX; Gibco, Cat# 36600021). U2OS cells were cultured in DMEM (1 g/L D-Glucose, Sodium Pyruvate, GlutaMAX; Gibco, Cat# 10567014). Media for all cell lines were supplemented with 10 % (vol/vol) heat-inactivated FBS (Bio&SELL, FBS Superior stabil) and 1 % antibiotics (penicillin–streptomycin, Bio&SELL). Cells were cultured at 37 °C, and 5 % CO2 under humidified conditions. Generally, cells were passaged at subconfluency every two to three days. Only cells under passage 20 were used for experiments. Monthly mycoplasma tests were conducted to rule out contamination.

5.3. Fluorescent Labelling of mitochondria for microscopy

For COS7 and U2OS cells, 35 mm μ -dishes (Ibidi) were coated overnight at 4 °C using 400 μ L poly-l-lysine solution (0.1 mg/mL, Cultrex). On the following morning, dishes were washed three times with sterile, double-distilled water (Milli-Q), and allowed to dry at room temperature (RT). Cells were seeded at a density of 2e5 cells per dish in complete culture medium (CCM). After 18 h of incubation at 37 °C, 5 % CO2 under humidifed conditions, media was replaced with fresh CCM and MitoTracker Deep Red FM (Invitrogen) was added to a final concentration of 100 nM. Following 25 min of staining at 37 °C, cells were washed two times with pre-warmed CCM, and, finally, incubated for one hour in fresh CCM to allow diffusion of the dye. HCT cells were seeded into a removable 8-well chamber (Ibidi, Cat#80841) on a custom made 25 x 75 mm2 no. 1.5H cover slip (knittelGLASSS, Cat#CG000001) with

a density of 2e4 cells per well. After two days, cells were stained with 100 nM MitoTracker Deep Red FM in fresh CCM for 10 min at 37 $^{\circ}\text{C}.$ Subsequently, cells were washed with CCM three times for 5 min at 37 $^{\circ}\text{C}.$

LF cells were seeded, one day prior to staining, at a density of 1e5 cells per well onto coverslips of 15 mm diameter in a 12-well plate. Mitochondria were labelled using 100 nM MitoTracker Orange for 20 min at 37 $^{\circ}$ C. Afterwards, cells were washed twice with pre-warmed CCM. To allow diffusion of the dye, cells were incubated for one hour at 37 $^{\circ}$ C, 5 $^{\circ}$ CO2, under humidified conditions in fresh CCM. Finally, cells were fixed using 4 $^{\circ}$ *para*-formaldehyde (PFA), washed three times in PBS, and mounted on a glass slide using ProLong Gold Antifade mounting medium (Invitrogen).

HeLa Tom20-mEGFP cells were seeded at a density of 5e4 cells per well into a 8-well chambe μ -slide. Mitochondria were labelled using 150 nM MitoTracker Deep Red FM for 25 min at 37 °C. After washing three times with pre-warmed CCM, cells were incubated with fresh CCM for 30 min at 37 °C. To induce mitochondrial fragmentation, cells were treated with CCCP at a final concentration of 10 μ M for 20 min at 37 °C. Following this incubation period, the CCCP-containing medium is aspirated, and the cells were fixed with 3.7 % PFA in CCM for 8 min at RT. Finally, cells were washed three times with PBS.

5.4. Microscopes and imaging parameters

COS7 live cell imaging was performed at 37 °C and 5 % CO2 on a Leica TCS SP8 gSTED 3x microscope (Leica Microsystems) equipped with a HC PL APO CS2 63x/1.40 OIL objective (Leica Microsystems). MitoTracker Deep Red FM was excited using the 633 nm white light laser line. Fluorescence emission light was collected using the HyD detector with filters passing light between 648 nm and 689 nm. Images were bidirectionally scanned at 600 Hz speed. Pixel size was set to 0.015 μm . Lines were averaged a total of eight times. HCT and HeLa Tom20-mEGFP imaging was performed on the Abberior INFINITY Line employing an IX83 inverse microscope (Olympus) equipped with a UplanXApo 60x/1.42 Oil $\infty/0.17/\text{OFN}26.5$ objective (Olympus). Detector wavelength window was set to 600 nm to 750 nm, 633 nm laser line, dwell time to 5 μ s and pixel size to 500 nm.

LF cells were acquired using a LSM 980 Airyscan 2 (ZEISS) inverse confocal laserscanning microscope equipped with a Plan-Apochromat 63x/1.40 Oil DIC M27 (ZEISS) objective. The 561 nm laser line was used for excitation, a 488/561 beam splitter employed, and emitted light detected using the GaAsP-PMT with the wavelength window set to 300 nm -735 nm. Scanned lines were averaged four times. Acquired images were processed using the superresolution processing module in Zen Blue 3.5).

U2OS cells were acquired using a ZEISS Elyra 7 microscope equipped with a Plan-Apochromat 63x/1.4 Oil DIC M27 (ZEISS) objective. The following parameters were used: 647 nm laser, camera exposure time of 50 ms, an LBF 405/488/561/742 beam splitter, and a 640 longpass filter. SIM reconstruction was performed with Zeiss Zen Black software.

5.5. Training and inference

To train our GAU-Net model, we employed the Adam optimizer with a learning rate of 0.0001, ensuring stable convergence while preventing gradient explosion. The training process was limited to 200 epochs, with early stopping implemented to mitigate overfitting. We utilized binary cross-entropy as the loss function, which effectively optimizes pixel-wise segmentation tasks. A batch size of 16 was chosen to balance computational efficiency and model generalization. To further enhance stability and learning efficiency, batch normalization was applied after each convolutional layer, which helps normalize activations and accelerate convergence. Additionally, model checkpointing was used to save the best-performing model based on validation loss, ensuring optimal model selection for inference. These training strategies contributed to

the robustness and effectiveness of GAU-Net in handling complex segmentation tasks across diverse imaging conditions.

5.6. Evaluation metrics

The quality and performance of the segmentation results obtained from the MitoSkel neural network architecture were evaluated with segmentation metrics, such as F1 Score, Accuracy, Dice coefficient, Precision, Specificity, and Jaccard Index (Intersection over Union). These metrics provide quantitative measures to assess the accuracy, precision, and overall effectiveness of the segmentation process, thus allowing a comprehensive analysis of the model performance [16–18].

Accuracy: This measures the proportion of correctly identified pixels (both true positives and true negatives) in the image.

$$Accuracy = \frac{TP + TN}{TP + TN + FP + FN} \tag{9}$$

Where TP = True Positives, TN = True Negatives, FP = False Positives, FN = False Negatives.

F1 Score: This is the harmonic mean of precision and recall, providing a balance between them.

$$F1Score = 2 \frac{Precision.Recall}{Precision + Recall}$$
 (10)

Where Precision = $\frac{TP}{TP+FP}$ and $Recall = \frac{TP}{TP+FN}$

IoU (Intersection over Union) Score: Also known as the Jaccard Index, this metric measures the overlap between the predicted segmentation and the ground truth.

$$IoU = \frac{TP}{TP + FP + FN} \tag{11}$$

Specificity: This measures the proportion of actual negatives that are correctly identified (i.e., the ability of the model to identify true negatives).

$$Specificity = \frac{TN}{TN + FP} \tag{12}$$

Precision: Also known as Positive Predictive Value, this assesses the proportion of positive identifications that were actually correct.

$$Precision = \frac{TP}{TP + FP} \tag{13}$$

Mean Absolute Error (MAE): In the context of image segmentation, MAE measures the average magnitude of errors between the segmented image and the ground truth, pixel by pixel.

$$MAE = \frac{1}{N} \sum_{i=1}^{N} |y_i - \widehat{y}_i|$$
 (14)

Where y_i is the true value, \hat{y}_i is the predicted value, and N is the total number of pixels.

CRediT authorship contribution statement

Soumaya Zaghbani: Writing – original draft, Validation, Software, Methodology, Formal analysis. **Rubaiya Kabir Pranti:** Writing – original draft. **Lukas Faber:** Resources, Data curation. **Ana J. Garcia-Saez:** Writing – original draft.

Declaration of competing interest

The authors declare that they have no known competing financial interests or personal relationships that could have appeared to influence the work reported in this paper.

Acknowledgments

This research was financed by the Alexander von Humboldt Foundation and partially by the CRC1218. The authors thank all our colleagues in García-Sáez group especially Dr.Timo Dellmann, Dr. Yasmine Abdelwahab, Lisa Hohorst, Jonas Aufdermauer, Cristiana Zollo and Julia Benecke who generously shared their expertise in working with cells and imaging techniques. We are particularly thankful to Dr. Katarzyna Bozek and her postdoctoral colleague Dr. Noémie Moreau for their insightful feedback and constructive criticism with the manuscript. We thank also Christian Jüngst, Felix Babatz, Katrin Seidel and Astrid Schauss of the CECAD Imaging Facility for helpful advice and technical support.

Data availability

Data will be made available on request.

References

- L. Tilokani, S. Nagashima, V. Paupe, and J. Prudent, "Mitochondrial dynamics: Overview of molecular mechanisms," Jul. 20, 2018, *Portland Press Ltd.* doi: 10.1042/FBC20170104.
- [2] P. S. Brookes, Y. Yoon, J. L. Robotham, M. W. Anders, and S. S. Sheu, "Calcium, ATP, and ROS: A mitochondrial love-hate triangle," Oct. 2004. doi: 10.1152/ ajpcell.00139.2004.
- [3] N. Ishihara, et al., Mitochondrial fission factor Drp1 is essential for embryonic development and synapse formation in mice, *Nat Cell Biol* 11 (8) (2009) 958–966, https://doi.org/10.1038/ncb1907.
- [4] S. M. Hickey et al., "Fluorescence microscopy—an outline of hardware, biological handling, and fluorophore considerations," Jan. 01, 2022, MDPI. doi: 10.3390/ cells11010035
- [5] A.J. Valente, L.A. Maddalena, E.L. Robb, F. Moradi, J.A. Stuart, A simple ImageJ macro tool for analyzing mitochondrial network morphology in mammalian cell culture, *Acta Histochem* 119 (3) (Apr. 2017) 315–326, https://doi.org/10.1016/j. acthis.2017.03.001.
- [6] A. Zahedi, et al., Deep Analysis of Mitochondria and Cell Health Using Machine Learning, Sci Rep 8 (1) (2018) Dec, https://doi.org/10.1038/s41598-018-34455-y.
- [7] C. Xiao, et al., Automatic mitochondria segmentation for EM data using a 3D supervised convolutional network, Front Neuroanat 12 (Nov. 2018), https://doi.org/10.3389/fnana.2018.00092.
- [8] M. A. Zuluaga, · S Kevin Zhou, D. Racoceanu, and L. Joskowicz, "Anne L. Martel · Purang Abolmaesumi · Danail Stoyanov · Diana Mateus ·." [Online]. Available: http://www.springer.com/series/7412.
- [9] C. H. Chu, W. W. Tseng, C. M. Hsu, and A. C. Wei, "Image Analysis of the Mitochondrial Network Morphology With Applications in Cancer Research," Apr. 13, 2022, Frontiers Media SA. doi: 10.3389/fphy.2022.855775.
- [10] A. Lounas, et al., A 3D analysis revealed complexe mitochondria morphologies in porcine cumulus cells, *Sci Rep* 12 (1) (2022) Dec, https://doi.org/10.1038/s41598-022-19723-2
- [11] A. Rizk, et al., Segmentation and quantification of subcellular structures in fluorescence microscopy images using Squassh, *Nat Protoc* 9 (3) (2014) 586–596, https://doi.org/10.1038/nprot.2014.037.
- [12] W. Song, et al., Assessing mitochondrial morphology and dynamics using fluorescence wide-field microscopy and 3D image processing, *Methods* 46 (4) (Dec. 2008) 295–303, https://doi.org/10.1016/j.ymeth.2008.10.003.
- [13] E. Lihavainen, J. Mäkelä, J.N. Spelbrink, A.S. Ribeiro, Mytoe: Automatic analysis of mitochondrial dynamics, *Bioinformatics* 28 (7) (Apr. 2012) 1050–1051, https://doi. org/10.1093/bioinformatics/bts073.
- [14] W. Weng, X. Zhu, INet: Convolutional Networks for Biomedical Image Segmentation, IEEE Access 9 (2021) 16591–16603, https://doi.org/10.1109/ ACCESS.2021.3053408.
- [15] K. Kavukcuoglu, P. Sermanet, Y.L. Boureau, K. Gregor, M. Mathieu, Y. LeCun, "learning Convolutional Feature Hierarchies for Visual Recognition," in Advances in Neural Information Processing Systems 23, Neural Information Processing Systems, 2010

- [16] O. Ronneberger, P. Fischer, T. Brox, "U-net: Convolutional networks for biomedical image segmentation," in Lecture Notes in Computer Science (including subseries Lecture Notes in Artificial Intelligence and Lecture Notes in Bioinformatics), Springer Verlag (2015) 234–241, https://doi.org/10.1007/978-3-319-24574-4_28.
- [17] C. A. Fischer et al., "MitoSegNet: Easy-to-use Deep Learning Segmentation for Analyzing Mitochondrial Morphology," iScience, vol. 23, no. 10, Oct. 2020, doi: 10.1016/j.isci.2020.101601.
- [18] S. Berg, et al., ilastik: interactive machine learning for (bio)image analysis, Nat Methods 16 (12) (Dec. 2019) 1226–1232, https://doi.org/10.1038/s41592-019-0582-9
- [19] K. Jaini and F. FARROKItNIAJ, "UNSUPERVISED TEXTURE SEGMENTATION USING GABOR FILTERS*," 1991.
- [20] M. Lyons, S. Akamatsu, M. Kamachi, and J. Gyoba, "Coding Facial Expressions with Gabor Wavelets.".
- [21] R. Mehrotra,', ~ K R Namuduri~, and N. Ranganathan, "GABOR FILTER-BASED EDGE DETECTION," 1992.
- [22] H. Xu, C. Liu, S. Duan, L. Ren, G. Cheng, B. Hao, A Fabric Defect Segmentation Model Based on Improved Swin-Unet with Gabor Filter, Appl. Sci. 13 (20) (Oct. 2023) 11386, https://doi.org/10.3390/app132011386.
- [23] A. Boughida, M.N. Kouahla, Y. Lafifi, A novel approach for facial expression recognition based on Gabor filters and genetic algorithm, *Evol. Syst.* 13 (2) (Apr. 2022) 331–345, https://doi.org/10.1007/s12530-021-09393-2.
- [24] S. Fekri-Ershad, Gender classification in human face images for smart phone applications based on local texture information and evaluated Kullback-Leibler divergence, *Traitement Du Signal* 36 (6) (2019) 507–514, https://doi.org/ 10.18280/ts.360605.
- [25] P. Alirezazadeh, M. Schirrmann, F. Stolzenburg, Improving Deep Learning-based Plant Disease Classification with Attention Mechanism, *Gesunde Pflanzen* 75 (1) (Feb. 2023) 49–59, https://doi.org/10.1007/s10343-022-00796-y.
- [26] S. Ghaffarian, J. Valente, M. Van Der Voort, B. Tekinerdogan, Effect of attention mechanism in deep learning-based remote sensing image processing: A systematic literature review, *Remote Sens (basel)* 13 (15) (2021) Aug, https://doi.org/ 10.3300/rs13152065
- [27] Z. Niu, G. Zhong, H. Yu, A review on the attention mechanism of deep learning, Neurocomputing 452 (Sep. 2021) 48–62, https://doi.org/10.1016/j. neucom.2021.03.091.
- [28] Y. Wang, Y. Li, and H. Zou, "Masked Face Recognition System Based on Attention Mechanism," *Information (Switzerland)*, vol. 14, no. 2, Feb. 2023, doi: 10.3390/ info14020087.
- [29] G. Liu, J. Guo, Bidirectional LSTM with attention mechanism and convolutional layer for text classification, *Neurocomputing* 337 (Apr. 2019) 325–338, https://doi. org/10.1016/j.neucom.2019.01.078.
- [30] Z. Zhou, M. M. R. Siddiquee, N. Tajbakhsh, and J. Liang, "UNet++: A Nested U-Net Architecture for Medical Image Segmentation," Jul. 2018, [Online]. Available: http://arxiv.org/abs/1807.10165.
- [31] J. Long, E. Shelhamer, and T. Darrell, "Fully Convolutional Networks for Semantic Segmentation," Nov. 2014, [Online]. Available: http://arxiv.org/abs/1411.4038.
- [32] V. Badrinarayanan, A. Kendall, and R. Cipolla, "SegNet: A Deep Convolutional Encoder-Decoder Architecture for Image Segmentation," Nov. 2015, [Online]. Available: http://arxiv.org/abs/1511.00561.
- [33] O. Ronneberger, P. Fischer, T. Brox, U-net: Convolutional networks for biomedical image segmentation, Lecture Notes in Computer Science (including Subseries Lecture Notes in Artificial Intelligence and Lecture Notes in Bioinformatics) (2015), https://doi. org/10.1007/978-3-319-24574-4 28.
- [34] C. J. Buswinka, H. Nitta, R. T. Osgood, and A. A. Indzhykulian, "SKOOTS: Skeleton oriented object segmentation for mitochondria," bioRxiv, 2023.
- [35] H. Yang, et al., Clueless/CLUH regulates mitochondrial fission by promoting recruitment of Drp1 to mitochondria, Nat Commun 13 (1) (2022) Dec, https://doi. org/10.1038/s41467-022-29071-4.
- [36] A. Rana, et al., Promoting Drp1-mediated mitochondrial fission in midlife prolongs healthy lifespan of Drosophila melanogaster, *Nat Commun* 8 (1) (2017) Dec, https://doi.org/10.1038/s41467-017-00525-4.
- [37] T. Trevisan, D. Pendin, A. Montagna, S. Bova, A.M. Ghelli, A. Daga, Manipulation of Mitochondria Dynamics Reveals Separate Roles for Form and Function in Mitochondria Distribution, *Cell Rep* 23 (6) (May 2018) 1742–1753, https://doi. org/10.1016/j.celrep.2018.04.017.
- [38] Y. Miyazono, S. Hirashima, N. Ishihara, J. Kusukawa, K.I. Nakamura, K. Ohta, Uncoupled mitochondria quickly shorten along their long axis to form indented spheroids, instead of rings, in a fission-independent manner, *Sci Rep* 8 (1) (2018) Dec, https://doi.org/10.1038/s41598-017-18582-6.
- [39] L. Laurien, et al., Autophosphorylation at serine 166 regulates RIP kinase 1-mediated cell death and inflammation, Nat Commun 11 (1) (2020) Dec, https://doi.org/10.1038/s41467-020-15466-8.